Comparison of Electrochemical Performance of Group IV and VI Elements in $ZnCo_2O_4$ as Symmetric Supercapacitors

By

CHARULATHA K

(20PPH004)

Supervisor

Dr.B. NALINI

Department of Physics

A Thesis submitted to

Avinashilingam Institute for Home Science and Higher Education for Women,
Coimbatore – 641043

In Partial Fulfilment of the Requirement for the Degree of

MASTER OF SCIENCE IN PHYSICS

MAY 2022

Comparison of Electrochemical Performance of Group IV and VI Elements in $ZnCo_2O_4$ as Symmetric Supercapacitors

By

CHARULATHA K

(20PPH004)

Supervisor

Dr.B. NALINI

Department of Physics

A Thesis submitted to

Avinashilingam Institute for Home Science and Higher Education for Women, Coimbatore – 641043

In Partial Fulfilment of the Requirement for the degree of

MASTER OF SCIENCE IN PHYSICS

MAY 2022

CERTIFIED AS A BONAFIDE THESIS WORK

27/05/22

Signature of the Head of the Department

27/05/2022

Signature of the supervisor

ACKNOWLEDGEMENT

I owe my sincere thanks to Lord Almighty and my parents for showering their generous blessings upon me in all endeavous.

I wish to express my gratitude to our chancellor, **Prof S.P.Thyagarajan,** Avinashilingam Institute for Home Science and Higher Education for Women, Coimbatore for providing all facilities to conduct this study.

I extend my thanks to **Dr. (Mrs) V.Bharathi Harishankar,** Ph.D., FRSA, Vice Chancellor, Avinashilingam Institute for Home Science and Higher Education for Women, Coimbatore, for providing flamboyant support towards the completion of the study.

I record my deep sense of gratitude and indebtedness to **Dr. (Mrs) S.Kowsalya,** M.Sc.,M.Phil., Ph.D., Registrar, Avinashilingam Institute for Home Science and Higher Education for Women, Coimbatore for her help rendered throughout the course of this work.

I also thankful to **Dr. (Mrs) G.Padmavathi,** M.Sc., M.Phil., Ph.D., Dean, School of Physical Sciences and Computational Sciences, Avinashilingam Institute for Home Science and Higher Education for Women, Coimbatore for granting the facilities required.

I whole heartily thanks to **Dr. (Mrs)J.Shanthi**, M.Sc., M.Phil., Ph.D., Professor and Head of the Department of Physics, Avinashilingam Institute for Home Science and Higher Education for Women, Coimbatore for her encouragement and generous help which was of great value.

I am also thanks to Dr. **(Mrs.) N. S. Rajeswari,** M.Sc., M.Phil., M.C.A., SLET, Ph.D., Assistant Professor-SG and former Head of the Department of Physics, Avinashilingam Institute for Home Science and Higher Education for Women, Coimbatore for her help and support.

I express my heartiest thanks to my guide **Dr. (Mrs)B.Nalini**, M.Sc., Ph.D., M.S(Edu.Mgt), STA fellow, AIST Fellow (Japan), Assistant Professor, Department of Physics, Avinashilingam Institute for Home Science and Higher Education for Women, Coimbatore for her inspiring guidance, meticulous care, patience, help, encouragement and motivation.

I express my gratitude to **(Mrs)G.G.Soundarya** and **(Mrs)P.Priyanka**, Research Scholars, Department of Physics, Avinashilingam Institute for Home Science and Higher Education for Women, Coimbatore for their valuable help in completion of my project.

I wish to express my special thanks to my parents, my friends and all my well-wishers for their constant encouragement, support and help in carrying out this work.

K. CHARULATHA

(20PPH004)

DECLARATION

I hereby declare that the project work entitled "**Comparison of Electrochemical Performance of Group IV and VI Elements in $ZnCo_2O_4$ as Symmetric Supercapacitors**" submitted to the Department of Physics, Avinashilingam Institute for Home Science and Higher Education for Women, Coimbatore, is a record of an original work done by me under the guidance of **Dr.(Mrs)B.Nalini,** Assistant Professor, Department of Physics and the project work is submitted in the fulfilment of the requirements for the degree of Master of Science in Physics. The results embodied in this have not been submitted to any other university or institute for the award of any degree or diploma.

K. Charulatha.

K. CHARULATHA

(20PPH004)

List of contents

	3.4.1.1 Principles of X-ray Powder Diffraction (XRD)	
	3.4.1.2X-ray Powder Diffraction (XRD) Instrumentation	
	3.4.1.3 Advantages	
	3.4.1.4 Strengths	
	3.4.1.5 Limitations	
	3.4.2 Field Emission Scanning Electron Microscopy (FESEM)	
	3.4.2.1 Principle of Operation	
	3.4.2.2 Instrumentation of FESEM	
	3.4.2.3 Advantages of FESEM include	
	3.4.2.4 Applications	
	3.4.3 Fourier Transform Infrared Spectroscopy (FTIR)	
	3.4.3.1 Principle of Operation	
	3.4.3.2 Instrumentation of FT-IR Spectrometer	
	3.4.3.3 Applications	
	3.4.3.4 Advantages	
	3.4.4 Raman Spectroscopy	
	3.4.4.1 Raman Spectroscopy Principle	
	3.4.4.2 Instrumentation of Raman spectrometer	
	3.4.4.3 Raman Spectroscopy Applications	

List of Figures

List of Tables

Chapter-1

Introduction

1.1. Introduction

There is increasing demand for portable and high-density energy storage devices to enable technological improvements and human life developments. Environmental change and consumption of petroleum products have unequivocally impacted the normal biological system and human economies (bio-economics). Environmental change and consumption of petroleum products have unequivocally impacted the normal biological system and human economies (bio-economics). In order to overcome these difficulties to create and design low-cost renewable sources and ecologically friendly storage and conservation of energy-related devices to encounter the increasing market demand for the improvement of convenient electronic and electric devices and vehicles. But, due to the climate changes, it is not easy to switch over from non-renewable resources to renewable resources. The solution of this problem lies in energy storage devices [1]. The first electrochemical capacitor device was patented by General Electric's H.I. Becker in 1957. Though double-layer charge storage was used with this device, it was impractical because of the need to immerse it in a pool of electrolytes. The potential to store electrical energy using an electric double layer at an interface between an electrolyte and solid compound has been known since the 19th century. However, it's been a struggle to create a reliable application for the technology. The supercapacitor has come a long way since conception, and recent technologies certainly prove useful applications for the age-old electrical design [2]. In recent years, researchers are focussing on energy storage devices such as supercapacitors (SCs) and lithium-ion batteries. Particularly, Supercapacitors are capable of providing a higher power density with an improved long-life than batteries and storing more than the conventional energy storage devices and are also called electrochemical capacitors or ultracapacitors. Though double-layer charge storage is used with this device, it is impractical because of the need to immerse it in a pool of electrolytes. The potential to store electrical energy using an electric double layer at an interface between an electrolyte and electrolyte has been studied since the 19th century. Generally, energy storage of the SCs depend on ionic adsorption (for electrical double-layer capacitors, EDLCs) or fast surface redox reactions (for pseudocapacitors). The combined electrode of EDLCs and pseudocapacitors form asymmetric supercapacitors, and they can extend the cell voltage. Besides, the combination of supercapacitors (EDLCs) and battery-type electrodes led to one more hybrid called

supercapattery (supercapacitor + battery) or hybrid supercapacitor, which performs as the power source and energy sourceAmong the energy storage devices, supercapacitors (SCs), exhibit outstanding properties such as high-power density, longer lifetime, cost-effective, ultrahigh charge-discharge rate, etc. In order to search for high energy and/or power density and longer cyclic stability electrode materials for SCs, much effort has centred on their rational design [3].

1.2. Supercapacitors:

Supercapacitors (SCs) are electrochemical devices and which is storing and supplying high-power electricity quickly and for a large number of cycles (up to millions of cycles) without showing performance decay. In SCs, the electrical charges are arranged in the electrode/electrolyte interface and there are no chemical oxidation-reduction processes. When a voltage is applied to a supercapacitor, two separate charge layers are produced on the surface with a separation distance that is smaller than those of conventional capacitors. Compared to conventional capacitors, supercapacitors have a larger area for storing more charge, with capacitance in farad (F) range and they store more energy than electrolytic capacitors. They have a low leakage current and are suitable for many applications that can operate in 1.8V - 2.5V range. The life of a supercapacitor is 10–20 years, though the capacity could be reduced from 100% to 80% after about 8–10 years. Thanks to their low equivalent series resistance (ESR), supercapacitors provide high load currents and fast charging. Micro-supercapacitors are MEMS-like devices that tolerate repeated bending and thus are suitable for flexible applications. This is ideal for wearables and IoT applications. Flexible solid-state micro-supercapacitor glass, silicon and paper substrates are being developed.

1.3. Types of Supercapacitors

Supercapacitors are classified into three types:

1. Electrostatic double-layer capacitors
2. Pseudo-capacitors
3. Hybrid capacitors

Electrostatic Double Layer Capacitors (EDLCs)

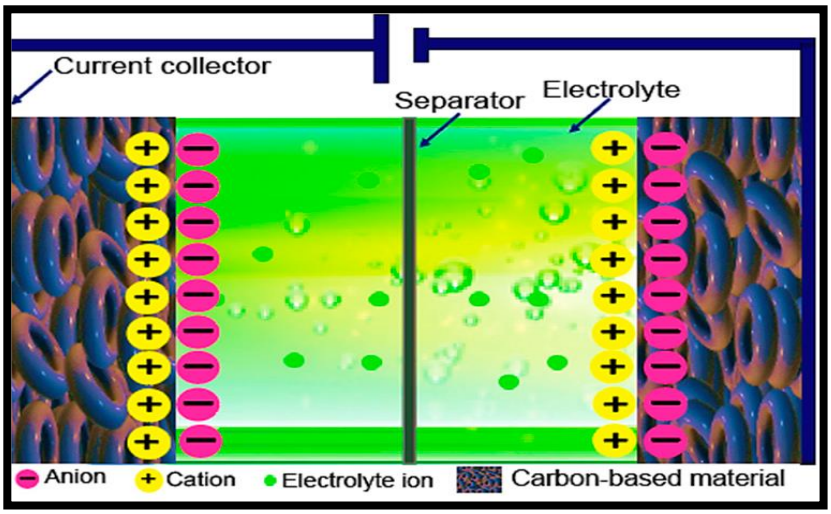

Figure 1.1: Electrical double-layer capacitors (EDLCs)

Based on their storage mechanism, supercapacitors can be classified into three types. The electric double layer supercapacitors include two electrodes, a separator and an electrolyte. The electrolyte is the mixture that constitutes positive and negative ions dissolved in water. The two electrodes are separated by a separator. These supercapacitors use carbon electrodes or derivatives with much higher electrostatic double-layer capacitance. The separation of charge in electrostatic double-layer capacitors is less than in a conventional capacitor; it ranges from 0.3–0.8 nm. The electrostatic double layer capacitors are shown in Figure 1.1.

Pseudocapacitors

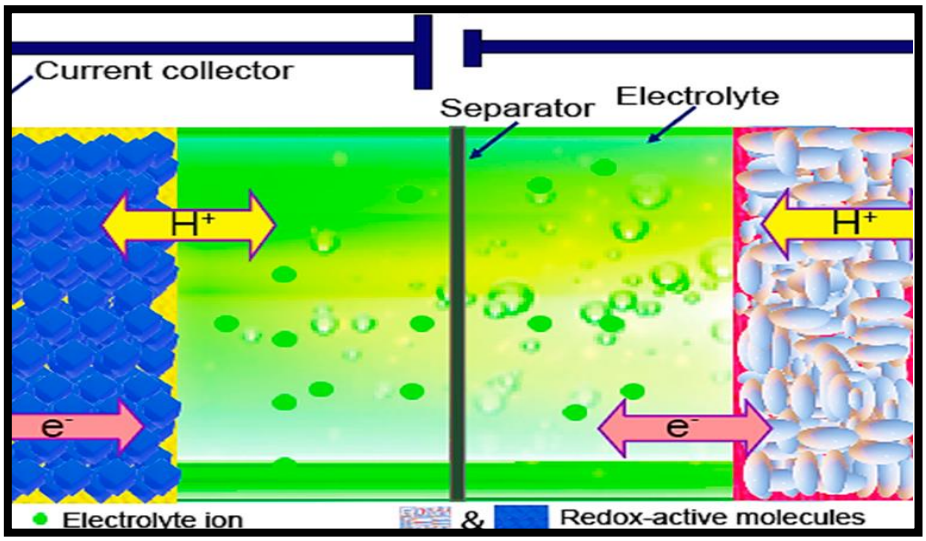

Figure 1.2: Pseudo capacitors

Pseudocapacitors are also referred to as electrochemical pseudo-capacitors as represented in Figure 1.2. These capacitors make use of metal oxide or conducting polymer electrodes with a high amount of electrochemical pseudo capacitance. These types of components store electrical energy by electron charge transfer between electrode and electrolyte. This can be done by a reduction-oxidation reaction commonly known as a redox reaction.

Hybrid capacitors

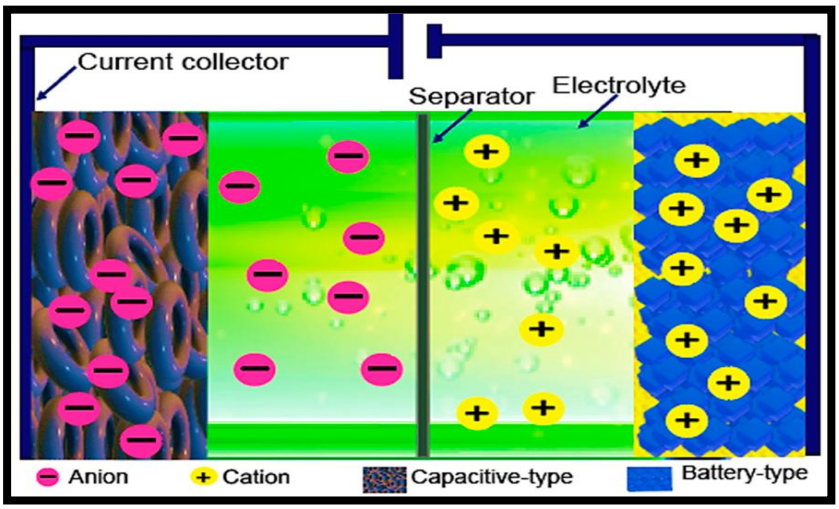

Figure 1.3: Hybrid supercapacitors (HSCs)

The hybrid capacitors are developed by using the techniques of double-layer capacitors and pseudo-capacitors as shown in Figure 1.3. In these components, electrodes with different characteristics are used. One electrode with the capacity to display electrostatic capacitance, and the other electrode with electrochemical capacitance. Examples of hybrid capacitors: the lithium-ion capacitor.

1.4 Electrode Materials for Supercapacitors

The advanced electrochemical properties, such as high energy density, fast charge–discharge rates, excellent cyclic stability and specific capacitance make supercapacitor a fascinating energy storage device. Due to this a significant amount of research has been done to enhance the electrochemical performance of the supercapacitors through the development of novel electrode materials. In addition to highlighting the charge storage mechanism of the three main categories of supercapacitors, including the electric double-layer capacitors (EDLCs), pseudo capacitors and the hybrid supercapacitors, this review describes the recent

electrode materials (including, carbon-based materials, metal oxide/hydroxide-based materials, and conducting polymer-based materials, 2D materials). These advanced properties provide a vast range of potential for the electrode materials to be utilized in different applications such as in wearable/portable/electronic devices such as all-solid-state supercapacitors, transparent/flexible supercapacitor and asymmetric hybrid supercapacitors [31]. The most common supercapacitor electrode materials, from 0D to 3D structures, are classified and shown in Figure 1.4

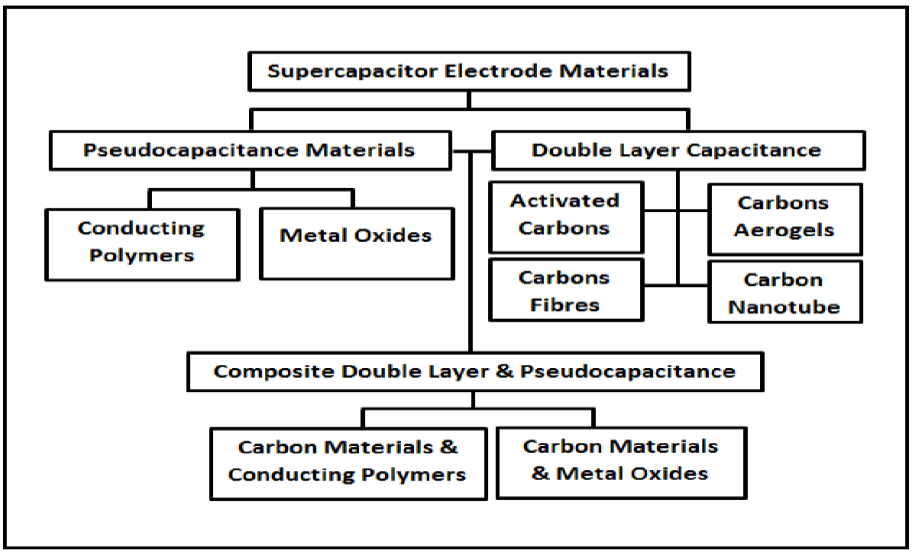

Figure 1.4: Common supercapacitor electrode materials from 0D to 3D structures

Carbon based electrodes

Carbon-based materials could be used in various forms such as powder, fibre, monoliths and foils in an SC device. In addition to pore shape and Specific Surface Area (SSA), there are other influential items such as the structure of the material, pore size distribution, and electrical conductivity that have an important consequence on the electrochemical performance of an SC device. There are several common examples of carbon-based material such as, carbon aerogels, graphene, activated carbon, activated carbon fibres (ACF), carbon nanotube (CNT), and carbon cloth (CC) as well as various carbon-based composites, which are suitable to be used as the electrode materials in SC devices.

Activated Carbon Materials (ACs)

Activated carbons are the most commonly used material for EDLC electrodes with moderate cost that show a complex porous structure comprising micropores (smaller than 2 nm), mesopores (in the range of 2–50 nm), and macropores larger than 50 nm that lead to having a high Specific Surface Area (SSA). Then their good electrical conductivities is lower (1250–2500 Sm^{-1}) and it is suitable for SCs. According to these properties, activated carbons are considered as useful electrode materials for SCs. Activated carbon can be produced in two steps involving either chemical or physical activation from various types of carbon-rich organic precursors such as fossil fuels, coke or synthetic polymers, wood, coconut shells. Activated carbon can be obtained from various carbon-rich organic precursors. The obtained coconut shell-based activated carbon exhibits supplementary micropores than the one which is made from charcoal. This shows that a slighter pore size distribution can be conveniently measured in the case of activated carbon fibre made from activated carbon with the surface area around 2500 m^2g^{-1}. Since the electrolyte ions with large size cannot enter in to the smaller micropores, for activated carbon, the whole Specific Surface Area (SSA) does not contribute to the charge storage mechanism. One of the significant disadvantages of activated carbon is its low density.

Carbon Nanotubes (CNTs)

Electrodes of CNTs have been developed due to their unique properties, such as their accessible external structure with high SSA and the specific internal work of mesopores, chemical and thermal stability, superior electrical conductivity and low mass densities. Then the mechanical flexibility of the Carbon Nanotubes (CNTs) and their open network provides them with a link to active material, higher interconnection and to form a continuous distribution that leads to the more utilized SSA. Carbon Nanotubes (CNTs) could be used as electrode material for SCs in the form of composite along with other materials such as graphene, metal oxides (MOs), polymer. Carbon Nanotubes (CNTs) can be classified into two main categories such as Single Walled Carbon Nanotubes (SWCNTs) and multi-walled carbon nanotubes (MWCNTs). Carbon Nanotubes (CNTs) materials could be deposited directly into the conductive substrates. In this case, the Carbon Nanotubes (CNTs) act as mechanical support, which increases electron transport, thus decreasing the contact resistance between the current collectors and active materials.

Graphene

Graphene is a one-atom-thick layered 2D structure with sp^2-bonded carbon atoms that is arranged in a honeycomb-designed crystal structure. Graphene, as a unique carbon material, which shows excellent features including superior mechanical, morphological characteristics, and electrical conductivity as well as high carrier mobility, large surface area and high chemical stability. Then, the 2D structure of graphene decreases the thickness of the electrode that leads to obtaining a larger potential window, greater flexibility, chemical, and thermal stability. Due to these properties, graphene is a powerful candidate for energy storage applications. Graphene could be utilized as electrode material in the application of high-performance SC, since, unlike other carbon-based materials such as ACs and CNTs, graphene-based electrodes do not depend on the distribution of pores in the solid-state. Another advantage of utilizing the graphene as an electrode material is the accessibility of both exterior surfaces of the graphene sheet by the electrolyte. There are plenty of methods to produce various types of graphene, such as micromechanical exfoliation, epitaxial growth, chemical vapour deposition, unzipping of CNTs, electrochemical and chemical approaches, arch discharge method and intercalation techniques in graphite. The graphene nanosheets (GNSs) could be used as electrode material for SC in 2D (also known as graphene paper), or 3D structure. In case of 2D graphene, the layer stacking could occur owing to the interplanar π - π interactions and van der Waals forces between the graphene sheets, which leads to a decrease in SSA, limiting the ion diffusion from the electrolyte, thus decrease in the electrochemical performance.

Metal based electrodes

In recent years, the harsh reality has generated a slew of social issues, prompting us to look for efficient ways to build high-performance supercapacitors**.** Hence, the researchers are focusing on binary transition metal oxides (BTMOs) as supercapacitor electrode materials due to their excellent electrochemical performance, inexpensive and environmental friendliness. When compared to single metal oxides, binary metal oxides (BTMOs) provide rich redox reactions and combine the contributions of two different types of ionic species. For example, the electrochemical activity of $NiCo_2O_4$ could be improved by substituting Ni for Co in the spinel Co_3O_4 lattice. As a result, BTMOs have sparked a lot of interest in supercapacitor applications.

Broad range of spinel structured metal oxides have been investigated for energy storage devices such as batteries and supercapacitors. Among the various reported spinel structured metal oxides, cobaltites (MCo_2O_4; M=Zn, Ni, Cu, Mn etc) have been considered as an efficient electrode material for supercapacitor applications due to its high electrochemical stability, abundant resources and low cost. For improving the electrochemical performance of cobaltites, several efforts have been attempted such as different nano-structured morphologies, doping with suitable elements, preparing the composite material etc.

1.5 Electrolyte for Supercapacitors

Electrolytes are one of the important constituents of electrochemical energy storage devices and their physical and chemical properties play an important role in these devices' performance, including capacity, power density, rate performance, cyclability and safety. Ionic mobility and conductivity are the important factors to calculate the performance of electrolytes. The conductivity of aqueous electrolytes is generally high as compared to that of non-aqueous and solid electrolytes due to the low dynamic viscosity of aqueous electrolytes. Among the capacitors, the double layer capacitors (DLC) are called the highest energy density and highest capacity per volume. Double layer capacitors store energy in so called Helmholtz double layers on the electrode's extension. The super or ultracapacitors that store electric energy not only electrostatically but also electrochemically by redox reaction on the electrodes which is higher specific capacity.

Aqueous Electrolyte

Aqueous electrolytes exhibit high conductivity as compared to organic and ionic electrolytes which is beneficial for lowering the equivalent series resistance and leads to better power delivery of SCDs. Materials whose working potential is located between the O_2 evolution potential and H_2 evolution potential are suitable for aqueous alkali-metal ion batteries. In addition, the electrode materials should be carefully selected with consideration of the pH, which is strongly associated with the O_2 and H_2 evolution potentials of an aqueous system. Aqueous electrolytes are divided into three categories: (1) alkaline, (2) neutral, and (3) acidic solutions. The most frequently used aqueous electrolytes are KOH, NaOH, LiOH, Na_2SO_4, H_2SO_4, $(NH_4)_2SO_4$ and K_2SO_4. Supercapacitors with high power density and life cycles are more important power suppliers in energy storage systems. The operating voltage window of a supercapacitor is derived by electrode materials and electrochemical kinetics of

electrolytes while the water hydrolysis potential is 1.23 V which is the typical limit for capacitors based on electrolytes. As far as the electrolytes are considered, aqueous electrolytes (such as KOH, H_2SO_4, Na_2SO_4 aqueous solution and so on) have the advantages of high-ionic conductivity, low cost, non-flammability, non-corrosiveness, safety, and convenient assembly in air compared to organic electrolytes which are believed to be less conductive, expensive, usually flammable and higher toxic. However, the potential window (~1.2 V) for aqueous electrolytes is far lower than that of organic electrolyte.

Non-aqueous Electrolyte

Nonaqueous electrolytes are applied in supercapacitors as they may provide electrochemical stability and they are able to combat the current leaking issue of the systems. Typical nonaqueous electrolyte systems are quaternary ammonium salts dispersed in carbonates or aceto-nitrile such as tetraethyl ammonium tetra fluoroborate/propylene carbonate, tetraethyl ammonium tetra fluoroborate/acetonitrile and triethyl methyl ammonium tetra fluoroborate/propylene carbonates. Besides, ionic liquids have been applied for supercapacitor due to their well-known characteristics of nonvolatility and nonflammability.

Gel polymer Electrolyte

Gel polymer electrolytes (GPEs) are being considered as an effective solution to replace currently available organic liquid electrolyte for building safer LIBs. Gel polymer electrolytes (GPEs) are preferred due to their higher safety and adaptability to the design of flexible energy storage devices. Gel polymer electrolyte absorb solvent constituents and aid in ion transport across the polymer matrix. The gel supports the polymer scaffold. That the amorphous domains of these polymers absorb larger amounts of solvent (and swell accordingly) than do crystalline domains. As a result, ion conduction which is primarily a diffusion-controlled process, is typically greater across regions of amorphous character through a crystalline domain. An important aspect of gel electrolytes are the choice of solvent primarily based on their dielectric constants which is the impact ion conductivity. Percolation of charge does occur in highly ordered polymer electrolyte but the number and proximity of amorphous domains are correlated with increased percolation of charge. Gel polymer electrolytes also find specific applications for lithium-ion batteries to replace current organic liquid electrolytes. This type of electrolyte has also been shown to be able to be prepared from renewable and

degradable polymers while remaining capable of mitigating current issues at the cathode-electrolyte interface.

1.6. Objective

- To incorporate Ba, Cs and K as dopants in the host lattice of $ZnCo_2O_4$.
- To analyse and compare the effect of dopants on the electrochemical performance when constructed as symmetric supercapacitor devices.

1.7. Methodology

- Preparation of doped Ba: $ZnCo_2O_4$ and doped Cs: $ZnCo_2O_4$ and K: $ZnCo_2O_4$ by sol-gel method.
- Characterize the prepared sample using various experimental techniques such as X-ray Diffractometer, Raman Spectroscopy, FT-IR Spectroscopy and FESEM
- Assembling the supercapacitor device with prepared electrode material
- Examine the electrochemical performance of the assembled supercapacitor device.

CHAPTER – 2

REVIEW OF LITERATURE

Introduction

The transitional metal oxides (TMOs)-based material is promising material due to its tunable chemical and physical properties. This review describes the progress of TMOs, namely zinc cobaltite ($ZnCo_2O_4$) for electrochemical devices. There are extensive researches that are ongoing based on their structure, application in energy storage devices and the development of cost-effective synthesis procedures. In this present work, the electrochemical performance of the Zinc cobaltite and device have been reviewed.

The $ZnCo_2O_4$ lilac flowers (LFs) are synthesized by using a rapid microwave irradiation method have reported by **Sreekanth et al., (2020)**. XRD analysis shows the ternary, spinel-based $ZnCo_2O_4$ LFs high crystallinity and high purity with no extra peaks. The stability of the $ZnCo_2O_4$ LFs was gained by using CV cycling testing, at the scan rate of 50 mVs^{-1}, for 500 cycles. Thus, the $ZnCo_2O_4$ LFs have superior durability and stability, which can be used to the strong coupling interactions between Zn and Co [4].

A dual-morphology $ZnCo_2O_4$ /N-doped reduced graphene oxide/Ni foam substrate (ZNGN) electrode by a one-step hydrothermal method have reported by **Wang et al., (2019)**. The crystal structure and the phase composition of the prepared samples are by XRD and cubic $ZnCo_2O_4$ phase. The electrochemical property shows that the potential application of the dual-morphology $ZnCo_2O_4$ electrode in supercapacitors. The electrochemical analysis shows the maximum capacitance of 1600Fg^{-1} at the current density of 1 Ag^{-1} in a 6 M KOH solution. This preparation method can stimulate the ability of materials can construct the complex structures with different morphologies at the nanometre scale that can be used in various energy-related applications [5].

The $ZnCo_2O_4$ electrode is prepared by a facial one-step hydrothermal method on a carbon cloth for the supercapacitor application have reported by **Patil et al., (2017)**. The maximum energy density of 12.5 $Whkg^{-1}$ is attained at a current density of 2 $mAcm^{-2}$ with the power density of 3.6 $kWkg^{-1}$ for the $ZnCo_2O_4$ micro strips electrode. And the 96.2 % capacitive

retention at a higher scan rate of 100 mVs^{-1} is observed after 1000 CV cycles, indicating excellent cycling stability of the $ZnCo_2O_4$ micro strips electrode. These result shows that the $ZnCo_2O_4$ micro strip architecture desirable for long term cyclic stability rate performance in the electrochemical application [6].

Free standing 3D hierarchical mesoporous $ZnCo_2O_4$ microspheres are grown on nickel foam (NF) substrate using hydrothermal route followed by annealing treatment have reported by **Wu et al., (2017)**. 3D hierarchical mesoporous $ZnCo_2O_4$ microspheres with high surface area and uniform mesoporous distribution exhibits high electrochemical performance. The $ZnCo_2O_4$/NF material exhibits the specific capacitance of 1143 Fg^{-1} at a current density of 1.25 Ag^{-1} in aqueous 2M KOH solution and exhibits long-term cycling stability with specific capacitance of 880 Fg^{-1} after 6000 cycles at 12.5 Ag^{-1} [7].

The $ZnCo_2O_4$ ultrathin nanosheets are obtained through a topological transformation approach have reported by **Bao et al., (2017)**. The Earth-abundant transition metal oxides materials with spinel structure has been intensively for pseudo capacitors and the device gives a high specific capacitance of 5100 $mFcm^{-2}$ and high energy density of 31.8 $mWhcm^{-3}$ at the power density of 280$mWcm^{-3}$. Hence, the high electrochemical performance shows that $ZnCo_2O_4$ ultrathin nanosheet is a prominent electrode candidate for both practical energy conversion and storage [8].

The hierarchical $ZnCo_2O_4$@MnO_2 core-shell nanosheet arrays and synthesized on Ni foam by a facile hydrothermal method have reported by **Yu et al., (2017)**. The fabricated $ZnCo_2O_4$@MnO_2 electrode exhibits a specific capacitance of 2170.00 Fg^{-1} (2.60 F cm^{-2}) at a current density of 3 $mAcm^{-2}$ in 1 M KOH solution. A current density of 10 mA cm^{-2} of the initial capacitance remained indicating its good cycling stability. All-solid-state ASC device gives a high energy density of 29.41 $Whkg^{-1}$ at a power density of 628.42 Wkg^{-1}. Thus, the hierarchical $ZnCo_2O_4$@MnO_2 core-shell nanosheet arrays on Ni foam shows a great potential for further applications in the energy storage field [9].

The $ZnCo_2O_4$, rGO and NiO using facile hydrothermal process followed by a short post annealing treatment have synthesized by **Sahoo et al., (2016**). The 3D ternary composite possesses an ultrahigh specific capacitance of 1,256 Fg^{-1} at a current density of 3 Ag^{-1} in 6 M KOH solution at a current density of 3 Ag^{-1}. Three-dimensional electrode exhibits superior

electrochemical performance, such as excellent cyclic stability (~ 80% capacitance retention after 3,000 cycles), maximum energy density of 62.8 $Whkg^{-1}$, maximum power density of 7,492.5 Wkg^{-1}, and low equivalent series resistance. These result shows that the prepared ZCGNO could be a superior candidate for the fabrication of binder free electrodes. It also shows that, the proposed synthetic strategy can be extended to the fabrication of other ternary binder free electrodes for next generation supercapacitor applications [10].

The pure $ZnCo_2O_4$ nanoparticles (NPs) are synthesized by using four different mass ratios of polyvinyl pyrolidone (PVP) with respect to metal oxides through a facile hydrothermal process**)** have reported by **Tomboc et al., (2016)**. In XRD, all the diffraction peaks can be indexed to cubic $ZnCo_2O_4$ with a spinel structure (JCPDS card no.23-1390). The highest specific capacitance of 1152.19 Fg^{-1} at a current density of 5 Ag^{-1}. The results show that PVP played a very important role in the formation of $ZnCo_2O_4$ NPs [11].

Porous $ZnCo_2O_4$ nanostructures by a facile hydrothermal route with HMT have prepared by **Xu et al., (2016)**. The asymmetric supercapacitor is fabricated using the $ZnCo_2O_4$ (anode) and freeze-dried reduced graphene oxide (FRGO) cathode and achieves a high cell voltage of 1.6 V and exhibits an ultrahigh energy density (84.48 $Whkg^{-1}$at 0.4 $kWkg^{-1}$). The obtained $ZnCo_2O_4$ nanostructures are further applied as electrode materials for supercapacitors and exhibit noticeable pseudocapacitive performance with high specific capacitance of 776.2 Fg^{-1} at 1 Ag^{-1} and good cycle stability (84.3% capacity retention at 3 Ag^{-1}). Hence the wide availability of $ZnCo_2O_4$, combined with material shows that $ZnCo_2O_4$ nanostructure can be an active material for many devices [12].

Mesoporous $ZnCo_2O_4$ microspheres by facile hydrothermal method have prepared by **Guo et al., (2015)**. The specific capacity still maintains a high value of 1256 $mAhg^{-1}$ after 100 cycles at a current density of 100 mAg^{-1} in the potential ranging from 0.01 to 3.0 V which is about 3.4 times larger than that of the commercial graphite electrode (372 $mAhg^{-1}$). The reversible capacity as high as 774 $mAhg^{-1}$ can be retained at a high current density of 1000 mAg^{-1} after 200 cycles, which indicates that the mesoporous $ZnCo_2O_4$ microspheres has the potential to be a high rate anode material for LIBs [13].

The urchin-like $ZnCo_2O_4$ microspheres that are prepared by a simple hydrothermal method have reported by **Wu et al., (2015**). The urchin-like $ZnCo_2O_4$-microspheres electrode

exhibits a high capacitance of 1841.8 F g^{-1} at a current density of 1 Ag^{-1} and keeps the capacitance retention about 78.4% at 10 Ag^{-1}. After 3000 cycles, the specific capacitance is about 1390.1 Fg^{-1} at a current density of 10 Ag^{-1}, and it also shows the excellent cycling stability (95.8%) [14].

The microspheres of $ZnCo_2O_4$ and prepared by facile hydrothermal method have demonstrated by **Huang et al., (2014)**. The prepared $ZnCo_2O_4$ exhibits a best cycling stability and highest specific capacity after the first charge and discharge process. The capacity of ZCO-s, ZCO-h and ZCO-cs maintains as high as 345, 831 and 985 $mAhg^{-1}$ after 50cycles. Then the anode materials for LIBs, the core-shell microspheres give a superior cycling stability [15].

The pineapple-shaped $ZnCo_2O_4$ (ZCO) microspheres with a porous nanostructure that are synthesized by a typical hydrothermal method have reported by **Guo et al., (2013**). The pineapple-shaped ZCO electrode exhibits a prominent rate performance, a reversible specific capacity of 1237 $mAhg^{-1}$ and 505 $mAhg^{-1}$ at current densities of 500 $mAg^{-1}$and 6000 mAg^{-1}. The application is limited by the large capacity fading due to the volume variations. The prepared pineapple-shaped ZCO sample show a high specific capacity, superior rate capability and excellent cycling stability when used as anode materials for LIBs [16].

The all-solid-state supercapacitors with assembling two pieces of the $ZnCo_2O_4$-based electrodes, showing superior performance in terms of high specific capacitance and long cycling stability have fabricated by **Liu et al., (2013)**. The high-performance supercapacitor based on hierarchical $ZnCo_2O_4$ nanorods/nickel foam architecture has been successfully fabricated, exhibiting a very high specific capacitance of 1400 Fg^{-1} at 1 Ag^{-1}, enhances rate capability and cycling stability (97 % retention after 1000 cycles at 6 Ag^{-1}). The result shows that the $ZnCo_2O_4$ of nano rods structure is highly desirable in the application of advanced electrochemical electrode materials, also open up the opportunities for the devices configuration for flexible electronics, high energy storage devices [17].

The $ZnCo_2O_4$ nanosheet arrays and prepared by a facile two-step method have reported by **Bao et al.., (2013**). The $ZnCo_2O_4$ nanosheet arrays/Ni foam electrode exhibits ultrahigh capacitance even with high current densities and excellent cycling stability after long term tests because of its unique nano structure. Hence, the structure and morphology of nanomaterials played an important role in determining the electrochemical performance of supercapacitor

materials and $ZnCo_2O_4$ with nanosheet arrays could be a great potential material for supercapacitors [18].

Author	Paper title	Preparation method	Result
Koyyada et al., (2021) [19]	In situ microwave-assisted solvothermal synthesis	Microwave assisted solvothermal synthesis method	XRD shows average crystallite sizes of about 18.8 and 16.9 nm. FESEM exhibits formation of 1D nanowires & 3D ZCO nano flowers on the nanoplates assist by Ni foam. Electrochemical performance of ZCO-15/Ni delivers an excellent specific capacity of 650.27Cg^{-1} at 0.5 $Ag^{-1}$and remarkable cyclic performance of 91% capacitance retention after 5000 cycles.
Priya et al., (2019) [20]	Structural and electrochemical properties of $ZnCo_2O_4$ nanoparticles synthesized by hydrothermal method	Hydrothermal method	The crystal structure of the $ZnCo_2O_4$ nanoparticles are identified by X-ray diffraction (XRD) technique. FESEM reveals that the synthesized product is of cubic structure. All-solid-state flexible supercapacitor is assembled based on the $ZnCo_2O_4$/rGO/sponge, which shows the specific capacitance of 143 Fg^{-1} at a current density of 1 Ag^{-1}.

Kumcham Prasad et al., (2019) [21]	Electrochemical Performance of 2D-Hierarchical Sheet-Like $ZnCo_2O_4$ Microstructures for Supercapacitor Applications	Hydrothermal method	XRD shows spinel and cubic phase of $ZnCo_2O_4$. SEM shows 2D hierarchical sheet-like morphologies of $ZnCo_2O_4$. Electrochemical performance of $ZnCo_2O_4$ electrode exhibits properties of areal capacitance of 16.13 mF cm^{-2} is deliveres at a current density of 10 μAcm^{-2} and shows good cycling performance of 170% capacitance retention and columbic efficiency of 135% after 1000 cycle at 500 μAcm^{-2}
Zhou et al., (2018) [22]	Controllable fabrication of $ZnCo_2O_4$ ultra-thin curved sheets on Ni foam for high-performance asymmetric supercapacitos	Hydrothermal method	XRD exhibits cubic $ZnCo_2O_4$ with a spinel structure. SEM shows nano array grew uniformly on the Ni foam in the presence or absence of the sodium dodecyl sulfate. Electrochemical performance of $ZnCo_2O_4$-UTCS electrode exhibits high specific capacity of 832 Cg^{-1} at 5 Ag^{-1}, remarkable high-rate capability (737 Cg^{-1} at 15 Ag^{-1}).

Shang et al., (2018) [23]	Synthesis of hollow $ZnCo_2O_4$ microspheres with enhanced electrochemical performance for asymmetric supercapacitor	Solvothermal method	XRD shows diffraction patterns assigned to cubic–$ZnCo_2O_4$. The $ZnCo_2O_4$//AC ASC displays a high energy density of 27.78 $Whkg^{-1}$ at a power density of 158.5 Wkg^{-1} and excellent stability with a capacitance retention of 178 % after 2000 cycles. The $ZnCo_2O_4$ exhibits a high specific capacitance of 78.89 $mAhg^{-1}$ at current density of 1 Ag^{-1} with a high loading of 6$mgcm^{-2}$ and superior cycling stability after 2000 cycles.
Xie et al., (2018) [24]	Core-shell structured $ZnCo_2O_4$@Z O_4 nanowire arrays on nickel foam for advanced symmetric supercapacitor	Hydrothermal method	XRD shows diffraction patterns assigned to cubic $ZnCo_2O_4$. The ASC device on $ZnCo_2O_4$@$ZnWO_4$//AC have been successfully fabricated, exhibiting a maximum energy density of 24 W h kg^{-1} at a power density of 400Wkg^{-1} and an energy density of 16.68 W h kg^{-1} at a high-power density of 2001.07Wkg^{-1}.
Zhu et al., (2017) [25]	Two-dimensional Porous $ZnCo_2O_4$ Thin Sheets Assembled by 3D Nanoflake	Hydrothermal method	XRD shows $ZnCo_2O_4$ with face-centred cubic structure. SEM shows $ZnCo_2O_4$ thin sheets composed of numerous nanoflakes array to form a porous 3D open network structure. Electrochemical performance of porous $ZnCo_2O_4$ thin sheets-

	Array with Enhanced Performance for Aqueous Asymmetric Supercapacitor		based electrode exhibits a high areal capacity of 3.07 F cm^{-2} at 1.04 m A cm^{-2}, and superior cycling stability (96.3 % of capacity retention after 5000 cycles at 10.4 mA cm^{-2}).
Katong Liu et al., (2017) [26]	Ni-doped $ZnCo_2O_4$ atomic layers to boost the selectivity in solar-driven reduction of CO_2 Capacitive Response	Hydrothermal method	XRD shows diffraction patterns assigned to cubic $ZnCo_2O_4$. FT-IR shows absence of organic matter on the surfaces and the formation of clean Ni- doped $ZnCo_2O_4$. DFT calculations to investigate the variation in the DOS
Ma et al., (2017) [27]	Role of N doping on the electrochemical performances of $ZnCo_2O_4$ quantum dots/reduced graphene oxide composite nanosheets	Solvothermal method	XRD exhibits face-centered cubic spinel crystal structure of $ZnCo_2O_4$. Series of tests indicated that the as-obtained $ZnCo_2O_4$/NG hybrids as a battery-type electrode for hybrid supercapacitor can deliver high specific capacity (301.8 C g^{-1} at 1Ag^{-1}), excellent rate capability (84.5% remaining at 30 Ag^{-1}), as well as outstanding cycle performance (89.1% after 5000 cycles).

Pan et al., (2017) [28]	Three-dimensional porous $ZnCo_2O_4$ sheet array coated with $Ni(OH)_2$ for high performance asymmetric supercapacitor	Hydrothermal method	Hierarchical $ZnCo_2O_4$@$Ni(OH)_2$ composite structure has been synthesized on Ni foam. The $ZnCo_2O_4$@$Ni(OH)_2$ composite electrode-based ASC device shows a maximum energy density of 49 Wh kg^{-1} at a power density of 428 W kg^{-1}.
V. Venkatachalam et al., (2017) [29]	Double hydroxide mediated synthesis of nanostructured $ZnCo_2O_4$ as high-performance electrode material for supercapacitor applications	Hydrothermal method	XRD exhibits cubic crystal system corresponds to spinel $ZnCo_2O_4$. FT-IR shows sharp peaks at 563 and 663 cm^{-1} are ascribed to Co–O and Zn–O stretching vibration and 1632 and 3447 $cm^{-1}$are attributed to O–H stretching and bending vibration mode of H–O–H group. Raman spectrum exhibits active mode at 193 cm^{-1} belongs to A–O stretching mode. Electrochemical performance of $ZnCo_2O_4$ electrode shows specific capacitance of 845.7 Fg^{-1} at a current density of 1 Ag^{-1} and cyclic stability of 95.3% capacitance retention after 5000 cycles at current density of 5 A g^{-1}.
Moon et al.., (2016) [30]	3D Hierarchically Mesoporous	Hydrothermal method.	$ZnCo_2O_4$/rGO/sponge electrode yields the highest specific capacitance of 1116.6 Fg^{-1}

	$ZnCo_2O_4$ Nanowires Grown on Graphene/Sponge Foam for High Performance Flexible All-Solid-State Supercapacitors		at the scan rate of 2 mVs^{-1} in 2 KOH aqueous electrolyte. The prepared all-solid-state supercapacitor exhibits a specific capacitance of 143 Fg^{-1} at a current density of 1 Ag^{-1}, 93.4% of the capacitance could still be maintained after 5000 cycles and can be used to fabricate a simple solid-state capacitive device with highly flexibility. The potential of $ZnCo_2O_4$/rGO/sponge is an electrode in flexible high-performance supercapacitors.
Zhang et al., (2015) [31]	Self-assembly of Mesoporous $ZnCo_2O_4$ Nanomaterials: Density Functional Theory Calculation and Flexible All-Solid-State Energy Storage	Hydrothermal method	XRD exhibits face-centred cubic spinel crystal structure of $ZnCo_2O_4$. The fabricated device shows superior capacity of 220.6 Fg^{-1} at a current density of 2 Ag^{-1} as well as long-term cycling stability with 67.5% capacitance retention after 8,000 cycles. The maximum energy density of 60.04 Wh kg^{-1} is reached at a power density of 1.4 KW kg^{-1} with an operating voltage of 1.4 V.
Zhou et al., (2014) [32]	Simple method for the preparation of highly porous $ZnCo_2O_4$nanotubes	Hydrothermal method	XRD exhibits peaks at well-defined planes of the $ZnCo_2O_4$. A simple strategy has been developed to fabricate $ZnCo_2O_4$ PNTs with high electrochemical

	with enhanced electrochemical property for supercapacitor		performance for SCs. $ZnCo_2O_4$ PNTs—shows a high specific capacitance of 770 Fg^{-1} at 10 Ag^{-1} with excellent rate performance (84% of the capacity retention at 60 Ag^{-1}) and high electrochemical reversibility and stability.
Guan et al.., (2014) [33]	Facile synthesis of $ZnCo_2O_4$ nanowire cluster arrays on Ni foam for high-performance asymmetric supercapacitors	Hydrothermal method	XRD shows the planes of cubic spinel structure of $ZnCo_2O_4$. The $ZnCo_2O_4$ Nanowire cluster arrays (NWCAs) on Ni foam is directly used as integrated electrodes for supercapacitors and exhibits a high specific capacitance of 4.05 Fcm^{-2} at 20 $mAcm^{-2}$ (1620 Fg^{-1} at 8 Ag^{-1}) in 3 M KOH aqueous solution, and an excellent cycling ability at various current densities up to 100 mA cm^{-2} (40 Ag^{-1}); 90% of the initial capacitance remained after 6000 cycles. The asymmetric supercapacitor has a high energy density of 41.00 $Whkg^{-1}$ at a power density of 384 Wkg^{-1} and 16.63 $Whkg^{-1}$ at a high-power density of 2561 Wkg^{-1}.

CHAPTER – 3

MATERIALS AND METHODS

3.1 Introduction

In this Chapter, method of preparation and characterization techniques like X-Ray diffraction (XRD), Raman Spectroscopy, Fourier Transform Infrared Spectroscopy (FTIR), Cyclic voltammetry (CV), Galvanostatic charge–discharge (GCD) have been discussed.

3.2 Materials used

- Zinc chloride dry ($ZnCl_2$)
- Cobalt (II) chloride hexa hydrate ($CoCl_2.6H_2O$) purified
- Barium chloride ($BaCl_2$)
- Citric acid monohydrate
- Cesium chloride ($CsCl_2$)
- Potassium chloride (KCl_2)

3.3 Method of preparation:

Barium doped Zinc cobaltite (Ba: $ZnCo_2O_4$), Cesium doped Zinc cobaltite (Cs: $ZnCo_2O_4$) and Potassium doped Zinc cobaltite (K: $ZnCo_2O_4$) has been prepared by sol gel method. In this method of preparation, the molar ratio of the Zinc chloride, Barium chloride, Cobalt (II) chloride hexa hydrate purified, Citric acid monohydrate is calculated by using the molecular weight of the precursor materials and solvent. A 0.8M of $ZnCl_2$ (1.090g) and 0.2M of $BaCl_2$ (0.4486g) is mixed with 20ml of distilled water and kept stirring until all the salts are dissolved. Then, 2M of $CoCl_2.6H_2O$ (4.758g) is mixed with 10 ml of DI water and added into the above solution. Finally, 1.33 M of citric acid monohydrate (2.794g) is mixed with the solution. Then the resultant solution is heated upto 80˚C to form a gel. The obtained gel is heated at 550˚C for 5 hours to get the powdered sample. Then prepared sample has been taken for further analysis. The similar procedure has been followed for the preparation of Cesium doped Zinc cobaltite (Cs: $ZnCo_2O_4$) and Potassium doped Zinc cobaltite (K: $ZnCo_2O_4$).

3.4 Characterisation techniques:

3.4.1 XRD:

X-ray powder diffraction (XRD) is a rapid analytical technique primarily used for phase identification of a crystalline material and can provide information on unit cell dimensions. The analysed material is finely ground, homogenized and average bulk composition is determined.

3.4.1.1 Principles of X-ray Powder Diffraction (XRD)

The Principle of X-ray diffraction is constructive interference of two monochromatic X-rays and a crystalline sample. The interaction of the incident rays with the sample produces constructive interference when conditions satisfy Bragg's Law

$$n\lambda = 2d \sin \theta$$

where, λ - wavelength of X-ray, d –the distance between the lattice planes, θ - diffracted angle, n is an integer that represents the order of reflections.

The diagram of Bragg's law is given in Figure 3.1. Bragg's law relates to the diffraction angle and the lattice spacing in a crystalline sample to the wavelength of the electromagnetic radiation. The diffracted X-rays are detected, processed and counted by scanning the sample in all directions in a range of 2θ angle of the lattice due to the random orientation of the powdered material.

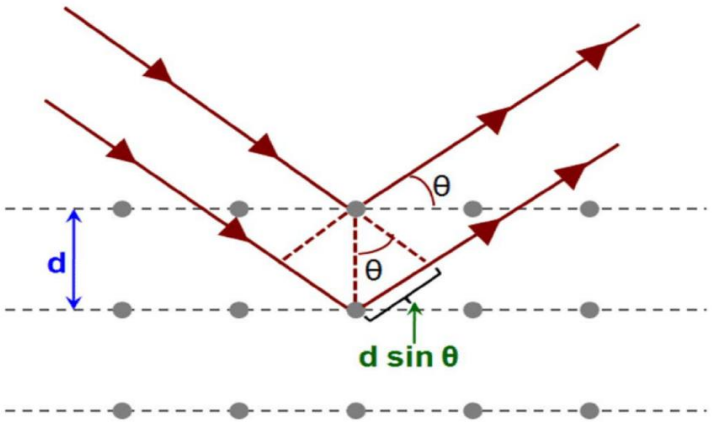

Figure 3.1: Schematic for understanding the principle of Bragg's law of X ray diffraction

3.4.1.2 X-ray Powder Diffraction (XRD) Instrumentation

X-ray diffractometers consist of three basic elements: An X-ray tube, a sample holder, and an X-ray detector. Figure 3.2 shows the Panalytical X-ray Diffraction instrument.

Figure 3.2: Photograph of Panalytical X-ray Diffraction instrument

X-rays are generated in a cathode ray tube by heating a filament to produce electrons, accelerating the electrons to impinge on a target by applying a voltage and bombarding the target material with electrons. Then the electrons have sufficient energy to dislocate inner shell electrons of the target material and characteristic X-ray spectra are produced. These spectra consist of some components, the most common component K_1 and K_2. K_1 consists of $K_{\alpha 1}$ and $K_{\alpha 2}$. $K_{\alpha 1}$ has a slightly shorter wavelength and twice the intensity as $K_{\alpha 2}$. The specific wavelengths are characteristic of the target material (Cu, Fe, Mo, and Cr). Filtering is done by foils or crystal monochromators and is required to produce monochromatic X-rays which is needed for diffraction. $K_{\alpha 1}$and $K_{\alpha 2}$ are sufficiently close in wavelength such that a weighted average of the two is used. Copper is the most common target material for single-crystal diffraction with CuK_{α} radiation = 1.5418Å. These X-rays are collimated and directed to the sample. As the sample and detector are rotated, the intensity of the reflected X-rays is recorded. A detector records and processes this X-ray signal and converts the signal to an count rate which is then fed to an output device such as a printer or computer monitor.

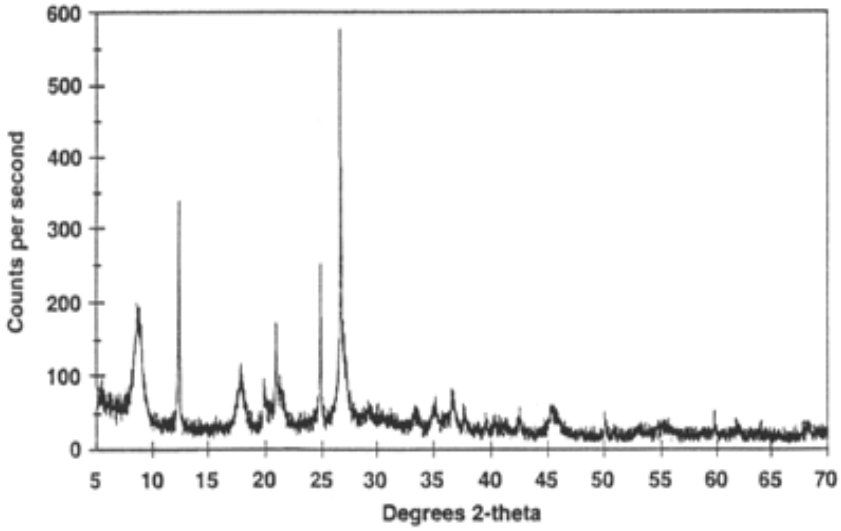

Figure 3.3: A Typical X-ray diffractogram.

The geometry of an X-ray diffractometer is such that the sample rotates in the path of the collimated X-ray beam at an angle θ while the X-ray detector is mounted on an arm to collect the diffracted X-rays and rotates at an angle of 2θ. The instrument used to maintain the angle and rotate the sample is termed as goniometer. Figure 3.3 shows the typical X-ray scan of the powder patterns. For typical powder patterns, data is collected at 2θ from ~5° to 70° and the data is interpreted. XRD can be used to determine crystal structures using Rietveld refinement, to determine the modal amounts of minerals (quantitative analysis), characterize thin films samples by determining lattice mismatch between film and substrate and to inferring stress and strain, determining dislocation density and quality of the film by rocking curve measurements, superlattices in multi-layered epitaxial structures, determining the thickness, roughness and density of the film using glancing incidence X-ray reflectivity measurements, make textural measurements, such as the orientation of grains, in a polycrystalline sample.

3.4.1.3 Advantages:

X-Ray diffraction is a powerful and rapid technique for the identification of unknown minerals and materials. It requires only a small amount of sample for analysis. X-Ray diffraction is comparatively straightforward on interpreting the data obtained.

3.4.1.4 Strengths

Powerful and rapid (< 20 min) technique for identification of an unknown mineral, in most cases, it provides an unambiguous mineral determination, Minimal sample

preparation is required, XRD units are widely available and Data interpretation is relatively straight forward.

3.4.1.5 Limitations

Homogeneous and single-phase material is best for identification of an unknown structure must have access to a standard reference file of inorganic compounds (d-spacings, *hkl* planes), Requires tenths of a gram of material which must be ground into a powder. For mixed materials, detection limit is ~ 2% of sample, For unit cell determinations, indexing of patterns for non-isometric crystal systems is complicated, Peak overlay may occur and get worsened at high angle 'reflections'.

3.4.2 Field Emission Scanning Electron Microscopy (FESEM)

Field emission scanning electron microscopy (FESEM) provides topographical and elemental information at magnifications of 10 to 300,000 with virtually unlimited depth of field. Compared with convention of scanning electron microscopy (SEM), Field emission SEM (FESEM) produces clearer, less electrostatically distorted images with spatial resolution down 1 to 1 1/2 nanometres.

Figure 3.4: Photograph of Field Emission Scanning Electron Microscopy (FESEM) instrument.

3.4.2.1 Principle of Operation

A Field-emission cathode in the electron gun of a scanning electron microscope provides narrower probing beams at low as well as high electron energy, resulting in both improved spatial resolution and minimized sample charging and damage for applications that demand the highest magnification possible.

3.4.2.2 Instrumentation of FESEM:

In standard electron microscopes, electrons are generated mainly by heating a tungsten filament but in field emission scanning electron microscope, cold source is used. The electron beam is focused on electromagnetic lenses like condenser lens, scan coils, stigmator coils and objective lens and condenser lenses that collimates the beam. The current in the condenser determines the diameter of the beam and the scan coils deflect the electron beam over the object according to a zigzag pattern. The formation of the image on the monitor occurs in synchrony with this scan movement. The objective lens focuses the electron beam on the object, so it needs to apply a greater force to deflect the electron beam. The stigmator coils correct the irregularities in x and y deflection of the beam to obtain a perfectly round-shaped beam. When the primary probe bombards the object, secondary electrons are emitted from the object surface with a certain velocity determined by the levels and angles at the surface of the object. The secondary electrons strike the scintillator that produces photons. The signal produced by the scintillator is amplified and transduced to a video signal and fed to a cathode ray tube in synchrony with the scan movement of the electron beam. The screen reflects the structure on the surface of the object and a digital image is generated which can be further processed. Figure 3.4 gives Field Emission Scanning Electron Microscopy (FESEM) instrumentation.

3.4.2.3 Advantages of FESEM include:

The ability to examine smaller-area contamination spots at electron accelerating voltages compatible with energy dispersive spectroscopy (EDS). Reduced penetration of low-kinetic-energy electron probes closer to the immediate material surface. High-quality, low-voltage images with negligible electrical charging of samples (accelerating voltages ranging from 0.5 to 30 kilovolts). Essentially no need for placing conducting coatings on insulating materials.

3.4.2.4 Applications:

Semiconductor device cross section analyses for gate widths, gate oxides, film thicknesses, construction details, Advanced coating thickness, structure uniformity determination, small contamination feature geometry and elemental composition measurement (if annexed with EDX).

3.4.3 Fourier Transform Infrared (FTIR) Spectroscopy

Fourier Transform Infrared (FTIR) Spectroscopy is a performance of qualitative and quantitative analysis of organic compounds and to determine the chemical structure of many inorganic compounds. The FTIR microscope accessory permits the analysis of samples as small as a few microns in diameter. Figure 3.5: Photograph of Fourier Transform Infrared (FTIR) Spectroscopy instrument.

Figure 3.5: Photograph of Fourier Transform Infrared (FTIR) Spectroscopy Instrument.

3.4.3.1 Principle of Operation

Because the chemical bonds absorb infrared (IR) energy at specific frequencies (wavelengths), the basic structure of compounds are described by the spectral locations of their IR absorptions. Present day FTIR spectrometers offer speedy and sensitive measurements that was impossible to achieve with earlier wavelength-dispersive instruments. This capability allows rapid analysis of micro samples down to the nanogram level in some cases, making the

FTIR unmatched as a problem-solving tool in organic analysis. The FTIR microscope accessory allows spectra from a few nanograms of material to be obtained very fast, with little sample preparation, resulting in more data at lower cost. In some cases, thin films of residue are identified with a sensitivity that provides or even exceeds surface analysis techniques based on electron or ion beams. As an analytical technique, FTIR has few sample constraints. Solids, liquids and gases can be accommodated. In addition, many contaminants present on reflective surfaces such as solder pads or printed circuitry are readily analysed in situ using the FTIR microscope in reflectance mode.

3.4.3.2 Instrumentation of FT-IR Spectrometer:

In the double beam spectrometer, the beam from the source is split into two and is directed through the sample cell and reference cell. The rotating sector mirror alternatively allows sample beam and reference beam. The detector receives the sample beam and reference beam alternatively and it measures the radiant energy by its heating effect. The radiation is allowed to fall on the photoconducting material and the conductivity of the material is measured continuously by the bridge network. When the sample absorbs radiation, there will be inequality in the two beams and a signal is produced. The signal is then fed to a high gain amplifier which amplifies the low intensity signal up to useable level used to move an attenuator which cuts down the radiation coming out of the reference beam until energy balance is restored. This is achieved by a motor that drives the comb into the reference beam when an absorbing band is encountered and out of the beam when the band is passed out. The comb movement is recorded by the pen which is coupled to the motor.

3.4.3.3 Applications:

FTIR analysis applications include:

- **Materials evaluation and identification**: Organic compounds, Structure of many inorganic compounds, Deformulations, Forensics, Material homogeneity.
- **Failure analysis:** Micro-contamination identification, Adhesive performance, Material delamination, Corrosion chemistry.
- **Quality-control screening:** “Good-to-bad” sample comparison, Evaluation of cleaning procedure effectiveness, Comparison of materials from different lots or vendors.

3.4. Advantages:

FT-IR has improved optical output because of a slit-free optical design, resulting in a high signal-to-noise ratio. The ability in obtaining data of multiple wavelengths simultaneously without scanning through moving grating or prism. The wavenumber resolution is improved by using a laser source for accurate digital signal sampling and extending the mirror movement in the interferometer. The wavenumber measurement range is extended by changing the light source, beam splitter and detector for the specific purpose, either far-IR or near-IR.

3.4.4 Raman Spectroscopy

Raman spectroscopy is a molecular spectroscopic technique that utilizes the interaction of light with matter to gain insight into a material's make up or characteristics, like FTIR. The information provided by Raman spectroscopy results from a light scattering process, whereas IR spectroscopy relies on absorption of light. Raman spectroscopy yields information about intra- and inter-molecular vibrations and can provide additional understanding about a reaction. Both Raman and FTIR spectroscopy provide a spectrum characteristic of the specific vibrations of a molecule ("molecular fingerprint') and are valuable for identifying a substance. However, Raman spectroscopy can give additional information about lower frequency modes, and vibrations that give insight into crystal lattice and molecular backbone structure.

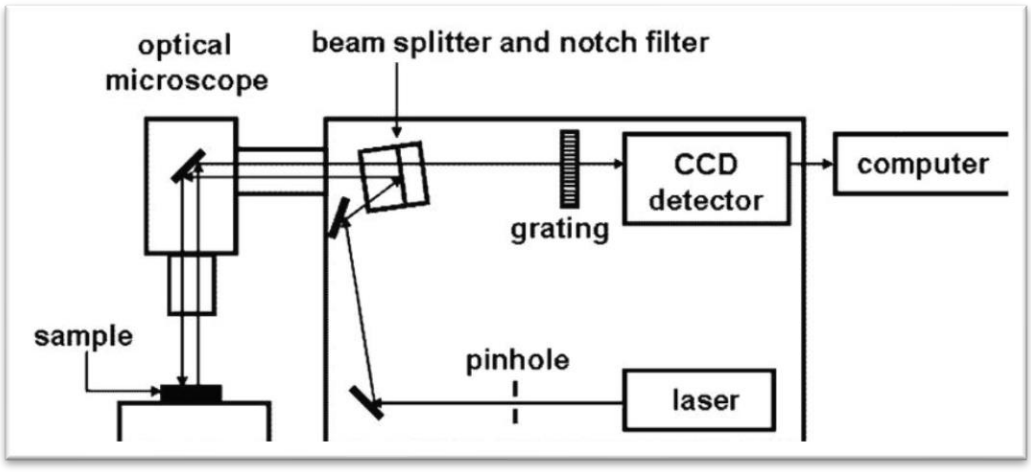

Figure 3.6 Block Diagram representation of Raman Spectrometer

3.4.4.1 Raman Spectroscopy Principle

When light interacts with molecules in a gas, liquid or solid, the vast majority of the photons are dispersed or scattered at the same energy as the incident photons. This is described as elastic scattering or Rayleigh scattering. A small number of these photons, approximately 1 photon in 10 million will scatter at a different frequency than the incident photon. This process is called inelastic scattering, or the Raman Effect, named after Sir C.V. Raman who discovered this and was awarded the 1930 Nobel Prize in Physics for his work. Since that time, Raman has been utilized for a vast array of applications from medical diagnostics to material science and reaction analysis. Raman allows the user to collect the vibrational signature of a molecule giving insight into how it is put together as well as how it interacts with other molecules around it.

3.4.4.2 Instrumentation of Raman spectrometer:

The first Raman spectrum uses Sun as a source and after that laser like He-Ne laser (632.8 nm), Argon ion laser (488 and 514.5 nm), krypton laser (647.1, 568.2, etc.,) and Argon krypton laser (488.0, 514.5, 647.1 nm) is used as the high intense sources. In most cases, the sample is placed outside the sample cavity. Two additional concave mirrors are used in sample illumination geometry and increase the observed intensity of scattering by 8-10 times. Filters and optical devices such as polarizer, polarization analyzer etc., may be inserted into the incident laser beam or the scattered beam. The monochromator often used is based on the grating. The dispersed radiation is detected photoelectrically. The exit slit allows a narrow band to reach the photomultiplier tube and the rotation of the grating allows the successive bands to reach the detector. The output of the photomultiplier tube is amplified and fed to the strip chart recorder. The detector used is Charged Coupled Device (CCD). Though Raman Effect is a weak phenomenon, the spectrograph-CCD combination used in unenhanced detection of material monolayers on a dielectric substrate.

3.4.4.3 Raman Spectroscopy Applications

Crystallization Processes, Polymorphism Identification, Polymerization Reactions, Hydrogenation Reactions, Chemical Synthesis, Bio catalysis and Enzymatic Catalysis, Flow Chemistry, Bioprocess Monitoring, Synthesis Reactions, Quality by Design are possible to detect with Raman analysis.

3.4.4.4 Advantages:

Many organic and inorganic materials like solids, liquids, polymers or vapours are suitable for Raman analysis and there is no need for special sample preparation. Raman spectrum in particular, like a chemical fingerprint of a material and can be acquired quickly within a second. A single recording can cover the region from 4000 cm^{-1} to 50 cm^{-1}. Raman spectra can be collected from a minimal volume of the sample and are easily analysable.

3.4.5 Electrochemical characterization

Electrochemical studies have several applications in multiple fields and hence a clear idea of the electrochemical characterization techniques is a must. So, in this chapter, various electrochemical characterization techniques (like voltametric techniques, impedance measurement technique and others) that are frequently used for electrochemical studies are discussed. All these techniques give a clear insight into the interfacial electrochemical behaviour between the electrode and the electrolyte (in an electrochemical cell). Hence, the techniques can be used to understand various electrochemical behaviours of materials. Some techniques even help to model the behaviour of a material by making an equivalent circuit of the same to replicate the behaviour. This is discussed using the Randles circuit.

3.4.5.1 Cyclic Voltammetry

Cyclic Voltammetry is an electrochemical technique for measuring the current response of a redox active solution to a linearly cycled potential sweep between two or more set values. It is a useful method for quickly determining information about the thermodynamics of redox processes, the energy levels of the analyte and the kinetics of electronic-transfer reactions. Like other types of voltammetry, cyclic voltammetry uses a three electrode system consisting of a working electrode, reference electrode and counter electrode. To perform cyclic voltammetry, the electrolyte solution is first added to an electrochemical cell along with a reference solution and the three electrodes. A Potentiostat is then used to linearly sweep the potential between the working and reference electrodes until it reaches a pre-set limit, at which point it is swept back in the opposite direction. This process is repeated multiple times during a scan and the changing current between the working and counter probes is measured by the device in real time. The result is a characteristic duck-shaped plot known as a cyclic voltammogram.

3.4.5.2 Experimental method

In cyclic voltammetry (CV), the electrode potential ramps linearly versus time in cyclical phases. The rate of voltage change over time during each of these phases is known as the experiment's scan rate (V/s). The potential is measured between the working electrode and the reference electrode, while the current is measured between the working electrode and the counter electrode. These data are plotted as current (*i*) versus applied potential (*E*, often referred to as just 'potential'). Thus, during the initial forward scan (from t_0 to t_1) an increasingly reducing potential is applied; thus, the cathodic current will, at least initially, increase over this time period, assuming that there are reducible analytes in the system. At some point after the reduction potential of the analyte is reached, the cathodic current will decrease as the concentration of reducible analyte is depleted. If the redox couple is reversible, then during the reverse scan (from t_1 to t_2), the reduced analyte will start to get re-oxidized, giving rise to a current of reverse polarity (anodic current) to the previous state. The more reversible the redox couple is, the more similar the oxidation peak will be in shape to the reduction peak. Hence, CV data can provide information about redox potentials and electrochemical reaction rates. For instance, if the electron transfer at the working electrode surface is fast and the current is limited by the diffusion of analyte species to the electrode surface, then the peak current will be proportional to the square root of the scan rate. This relationship is described by the Randles–Sevcik equation. In this situation, the CV experiment only samples a small portion of the solution, i.e., the diffusion layer at the electrode surface.

3.4.5.3. Electrode preparation

For electrochemical characterizations such as cyclic voltammetry (CV), Galvanostatic charge-discharge (GCD) and electrochemical impedance analysis (EIS), the working electrode has been prepared. In the preparation of working electrode, 85 wt.% of active material (Ba: $ZnCo_2O_4$, Cs: $ZnCo_2O_4$ and K: $ZnCo_2O_4$), 10 wt.% of conductive material (carbon black) and 5wt.% of binder (PVdF) is mixed together with NMP solvent to form a homogeneous slurry. Then, the resultant slurry is coated on the copper current collector and dried at 80^oC for 6hrs to evaporate the NMP in the working electrode.

3.4.5.4. Symmetric supercapacitor assembly

The all-solid-state symmetric supercapacitor is fabricated by assembling two pieces of prepared $ZnCo_2O_4$-based electrodes. A PVA/KOH composite gel electrolyte is prepared by mixing PVA powder (2 g), KOH (2 g), and deionized water (40 mL) and then heating to 60°C

under vigorous stirring until the solution becomes homogeneous. Then, the separator (cellulose acetate filter paper) is soaked with the above solution for 1 min and placed between two pieces of electrodes.

In the two-electrode configuration, the cyclic voltammetry, (CV) galvanostatic charge/discharge of devices and electrochemical impedance analyse are performed to analyze the performance of the device.

CHAPTER – 4

RESULTS AND DISCUSSION

4.1 Introduction:

This chapter deals with the analysis of the synthesized Barium doped $ZnCo_2O_4$ (Ba: $ZnCo_2O_4$), Cesium doped $ZnCo_2O_4$ (Cs: $ZnCo_2O_4$) and Potassium doped $ZnCo_2O_4$ (K: $ZnCo_2O_4$) using sol-gel method. The structural, morphological, vibrational and electrochemical properties of the prepared samples are characterized using XRD, RAMAN, FT-IR, FESEM analysis. The fabricated symmetric devices have been analyzed by CV, GCD and EIS techniques and the corresponding results have been discussed in this chapter.

4.2 X-Ray Diffraction Analysis:

The XRD patterns obtained for Ba: $ZnCo_2O_4$, Cs: $ZnCo_2O_4$, K: $ZnCo_2O_4$ are given in Figure 4.1. The background of XRD patterns are corrected by using Baseline tool from Origin software. The diffraction peaks observed for Ba: $ZnCo_2O_4$, Cs: $ZnCo_2O_4$ and K: $ZnCo_2O_4$ corresponds to the hkl planes of $ZnCo_2O_4$ spinel structure and matched with the standard JCPDS Card No: 23-1390. The 2θ values seen from all the three samples are assigned to the hkl values of (220), (311), (222), (400), (422), (511), (440), and (533) respectively. The parameters calculated from the XRD pattern at high intense peak for all the three samples are listed in Table 4.1.

Parameters from XRD:

Crystallite size D, can be estimated from the peak width using Scherrer's formula,

$$D = K\lambda/\beta COS\theta \quad (1)$$

Where, λ is the X-ray wavelength, β is the full-width half maximum (FWHM) of a diffraction peak, θ is the diffraction angle, K is constant (0.89).

Strain can be calculated from the formula

$$\varepsilon = \beta/4tan\theta \quad (2)$$

Dislocation density is calculated using the Williamson-Hall relation,

$$\delta = 1/D^2 \quad (3)$$

From Table 4.1, it is noted that the calculated crystallite size of the Barium (Ba) doped Zinc cobaltite is higher than the Cesium (Cs) and Potassium (K) doped Zinc cobaltite. It is due

to the lowest value of full width half maximum value observed in the barium doped zinc cobaltite sample. Hence, Ba: $ZnCo_2O_4$ sample shows the sharp X-ray diffraction peaks when compared to the Cesium and Potassium doped Zinc cobaltite, shown in Figure 4.1.

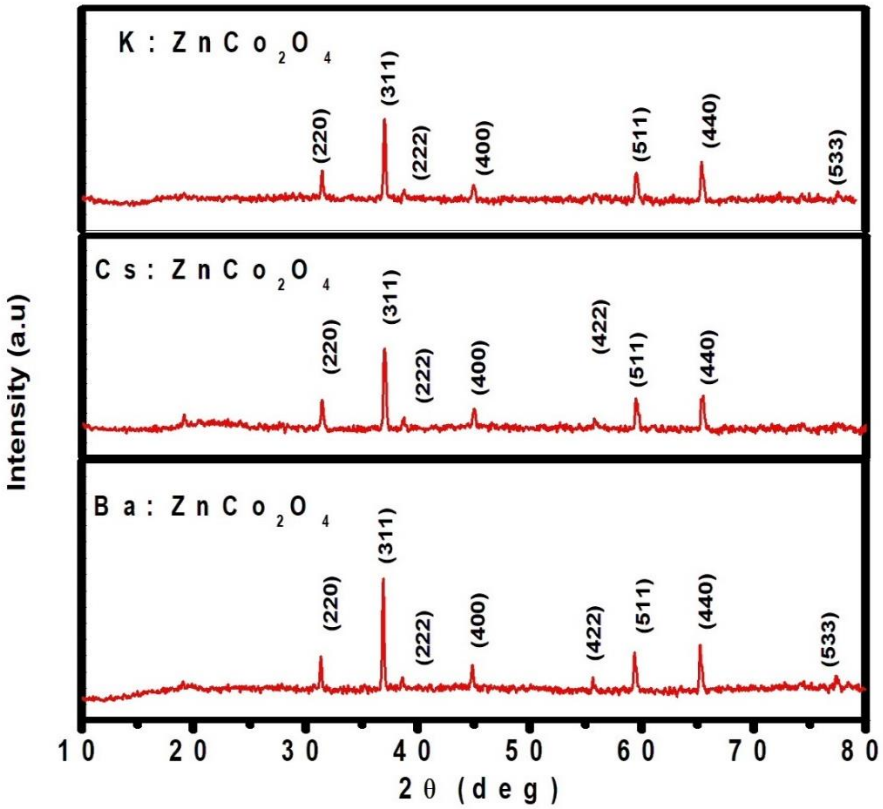

Figure 4.1: XRD pattern of Ba: $ZnCo_2O_4$, Cs: $ZnCo_2O_4$, K: $ZnCo_2O_4$ (by using Baseline tool from Origin software)

Table: 4.1 Crystallite size, strain and dislocation density calculated from the XRD

S. No	2θ (deg)	β (FWHM) (deg)	Crystallite Size (nm)	Strain	Dislocation density ($x10^{15}$) /cm^3
1.	36.69	0.15	52	0.1131	0.369
2.	37.17	0.23	34	0.1713	0.865
3.	37.00	0.23	34	0.1708	0.865

4.3 Raman Analysis:

The formation of spinel structured Ba, Cs and K doped Zinc cobaltite is further confirmed by Raman analysis and is shown in Figure 4.2a. In general, pure Zinc cobaltite has five Raman active bands. i.e., 193 cm^{-1} ($F_{2g}(3)$), 476 cm^{-1} (E_g), 516 cm^{-1} ($F_{2g}(2)$), 610cm^{-1} ($F_{2g}(1)$) and 682 cm^{-1} (A_{1g}) in the full region between 200 and 1000 cm^{-1}[36]. According to group theory, there are four letters i.e., A, B, E and T, that can be assigned to the vibrational modes of Raman analyses. A and B are related to the vibration of singly degenerate. E and T are related to the doubly degenerate and triply degenerate. In addition to this, F are related to the threefold degenerated mode of vibration. In the $ZnCo_2O_4$, doubly degenerate and threefold degenerate mode of vibration is presented and the corresponding pictorial representation is shown in 4.2b. The Raman F_{2g} mode at 510 cm^{-1} is attributed to Co-O the stretching mode in $ZnCo_2O_4$. The band at 476 cm^{-1} is attributed to E_g mode, indicating strong vibration related to the stretching of the bonds between Co-O and Zn-O.

Table 4.2 shows the Raman of active modes of Ba, Cs and K doped Zinc cobaltite. From Table 4.2, it can be concluded that the prepared samples exist in the spinel structure and in well agreement with the XRD analysis of pure $ZnCo_2O_4$ also. However, the Raman peaks observed from Ba, Cs and K doped Zinc cobaltite are shifted, compared to the Zinc cobaltite.

In Ba: $ZnCo_2O_4$, there is a splitting of peak in the range 690 cm^{-1}. The band at 692 cm^{-1} reveals A_{1g} mode with a Raman shoulder peak at 715 cm^{-1} to which again the vibrational mode is assigned. The splitting and shifting occurred in the prepared material may due to the effect of doping Ba, Cs and K into Zinc cobaltite that brought in changes in the structural parameters of the samples.

The Raman Spectroscopy theory is the idea that molecules can vibrate. The vibrational modes of a molecule can be modelled by assuming that the compound is composed of atoms (balls) joined by chemical bonds composed of springs (rather than the traditional sticks). When viewed in this way, it becomes apparent that an input of energy into the molecule will cause the molecule to vibrate. Vibrational modes for the molecule are a function of the orientation of its atoms and bonds, the atomic mass of the atoms, bond order and hydrogen bonding are few among other factors. Figure 4.2b shows the Modes of vibrations in Raman analysis.

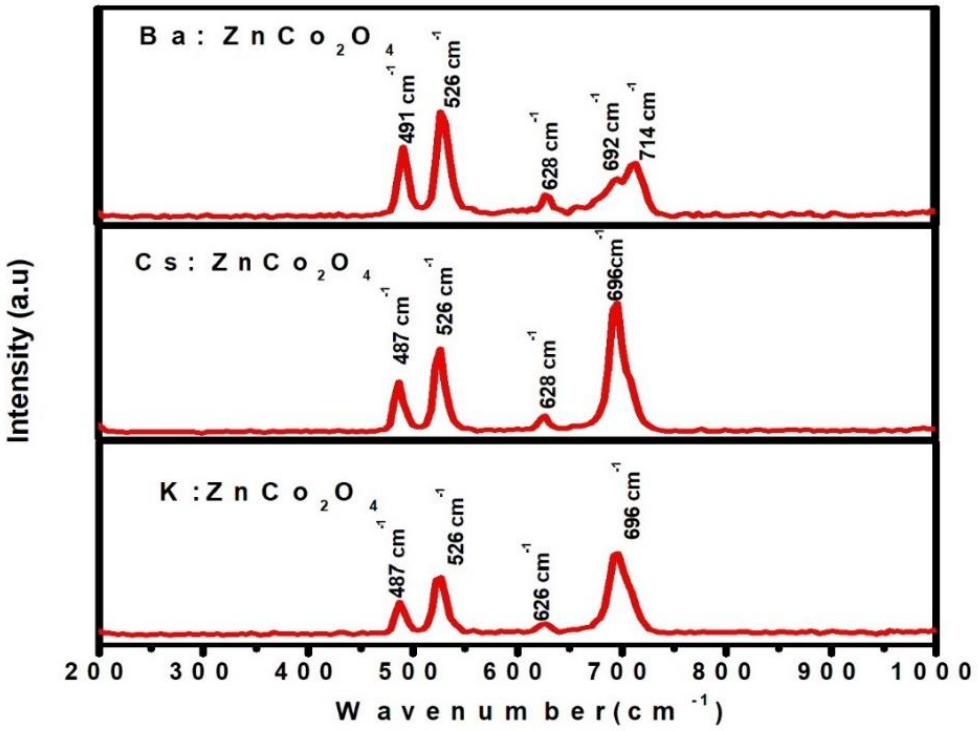

Figure 4.2a: Raman Spectrum of Ba: $ZnCo_2O_4$, Cs: $ZnCo_2O_4$, K: $ZnCo_2O_4$ sample

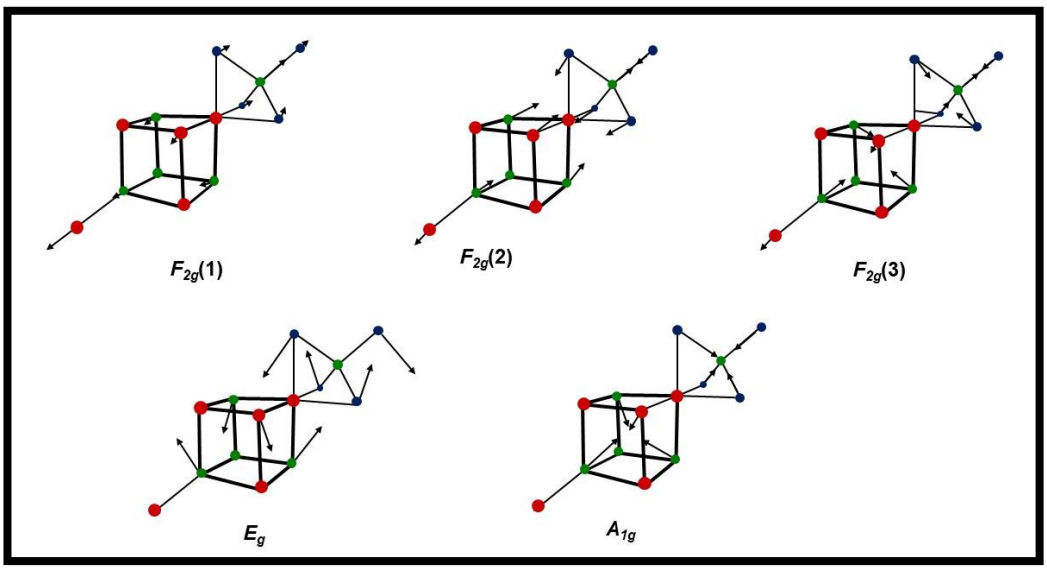

Figure 4.2b- Modes of vibrations in Raman analysis

Table 4.2 Raman of active modes for Ba: $ZnCo_2O_4$, Cs: $ZnCo_2O_4$, K: $ZnCo_2O_4$ sample

Sample	Raman band (cm^{-1})	Symmetry species	Assignment
Ba: $ZnCo_2O_4$	**491**	**E_g**	Stretching of the bonds between Co-O and Zn-O
	526	**F_{2g} (2)**	stretching of the Co-O bond
	628	**F_{2g} (1)**	Co-O bond stretching
	692	**A_{1g}**	Co-O bond stretching
Cs: $ZnCo_2O_4$	**484**	**E_g**	stretching of the bonds between Co-O and Zn-O
	523	**F_{2g} (2)**	stretching of the Co-O bond
	626	**F_{2g} (1)**	Co-O bond stretching
	699	**A_{1g}**	Co-O bond stretching
K: $ZnCo_2O_4$	**487**	**E_g**	stretching of the bonds between Co-O and Zn-O
	526	**F_{2g} (2)**	stretching of the Co-O bond
	626	**F_{2g} (1)**	Co-O bond stretching
	696	**A_{1g}**	Co-O bond stretching

4.4 Fourier Transform Infrared Spectroscopy (FTIR):

The FTIR spectrum of the synthesized Ba: $ZnCo_2O_4$, Cs: $ZnCo_2O_4$, K: $ZnCo_2O_4$ sample from 400 to 4000 cm^{-1} are shown in Fig.4.3a. For clear view, the low wavenumber region is zoomed and the corresponding graph is seen in Fig 4.3b. The sharp peak in the range of 550 -591 cm^{-1} and 645-650 cm^{-1} corresponds to the octahedral and tetrahedral site of Co-O and Zn-O stretching vibrational modes which confirms the formation of spinel Zinc cobaltite. The peak at 1615 cm^{-1} is ascribed to the stretching of CO bonds present in K: $ZnCo_2O_4$ the

sample [26]. The presence of CO vibrations of organic molecules are due to the traces of citric acid present in the sample. In Ba: $ZnCo_2O_4$ and K: $ZnCo_2O_4$, the peak appeared at 1630 cm^{-1} is due to the bending vibration of OH group. Table 4.3 gives FTIR bond assignment for the Ba: $ZnCo_2O_4$, Cs: $ZnCo_2O_4$, K: $ZnCo_2O_4$ samples.

The band located at 451cm^{-1} which is assigned to Zinc oxide character in the mixed spinel structure by Shaheen et al., [32] seem to get altered in Cs and Ba doped samples. It is to be noted that K doped has no such variation which may be due to regular (A-O-B) occupation of Cs and K. Cs and K being monovalent the occupation site is similar and hence nearly 451cm^{-1} is maintained. In contrary, significant change in this wave number with divalent dopant Ba may be due to the change in occupation as suggested by the Azouaoci et al.,[32] through their density functional calculation where the occupation sites of the dopant and Co might have exchanged.

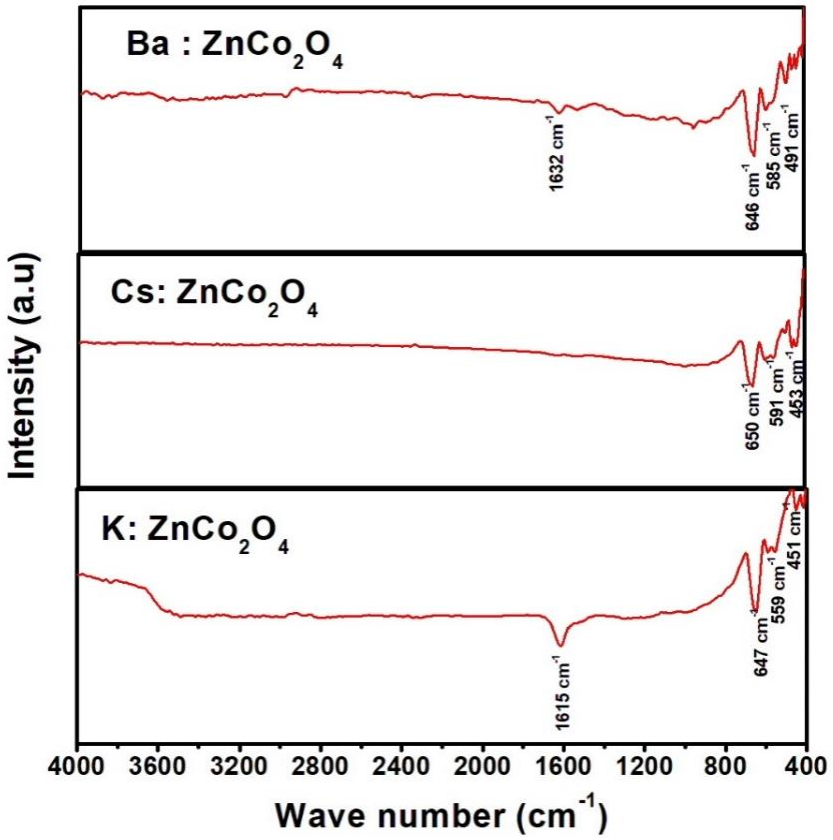

Figure 4.3a: FTIR spectra of the Ba: $ZnCo_2O_4$, Cs: $ZnCo_2O_4$ and K: $ZnCo_2O_4$ sample

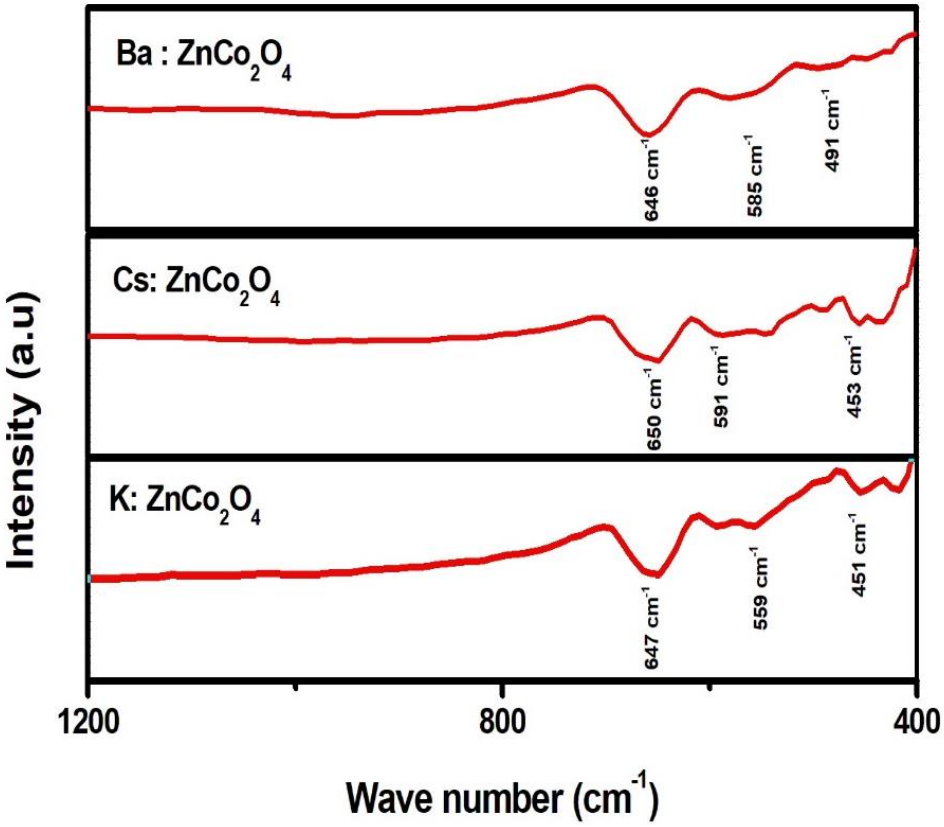

Figure 4.3b: FTIR spectra of the Ba: $ZnCo_2O_4$, Cs: $ZnCo_2O_4$ and K: $ZnCo_2O_4$ sample in high frequency region

Table 4.3 FTIR bond assignment for the Ba: $ZnCo_2O_4$, Cs: $ZnCo_2O_4$, K: $ZnCo_2O_4$

Sample	Wavenumber (cm^{-1})	Bond Assignment	Mode of Vibration
Ba: $ZnCo_2O_4$	585	Co-O	Stretching
	646	Zn-O	Stretching
Cs: $ZnCo_2O_4$	591	Co-O	Stretching
	650	Zn-O	Stretching
K: $ZnCo_2O_4$	559	Co-O	Stretching
	647	Zn-O	Stretching

4.5 Morphological Characterization

Morphological features of Ba: $ZnCo_2O_4$, Cs: $ZnCo_2O_4$ and K: $ZnCo_2O_4$ observed from FESEM are shown in Figure 4.4 (a-c) respectively. All the micrographs exhibit heterogeneous grain distribution showing a grain growth in the prepared samples. Micrographs of Ba: $ZnCo_2O_4$, Cs: $ZnCo_2O_4$ and K: $ZnCo_2O_4$ reveal the spinel shaped and assorted grain sizes. The grain size of all the prepared sample is in micrometer range.

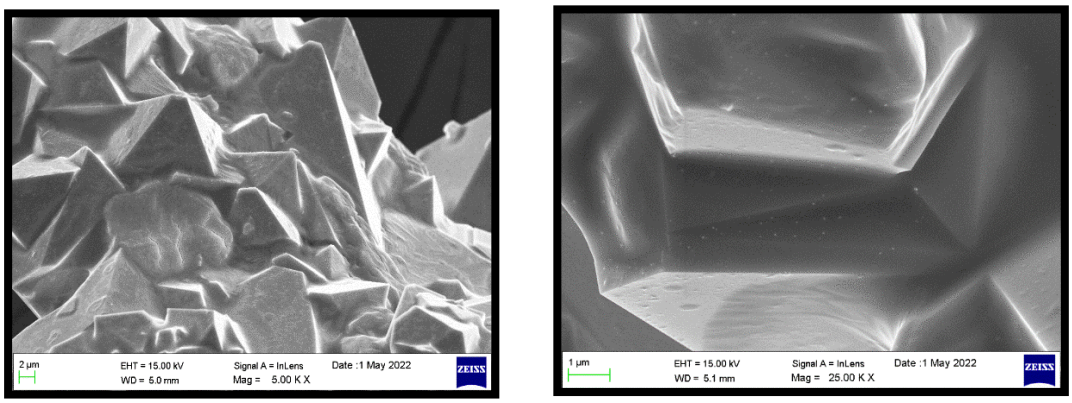

Figure 4.4a: FESEM micrographs of Ba: $ZnCo_2O_4$

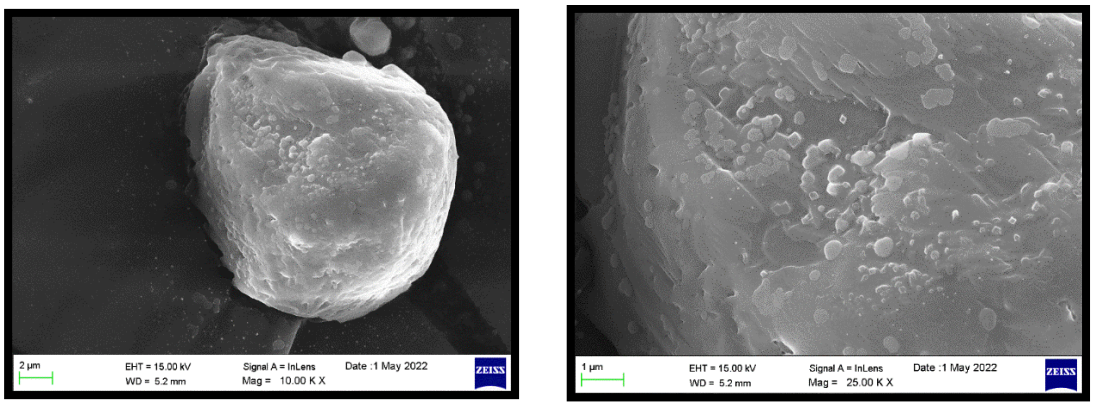

Figure 4.4b: FESEM micrographs of Cs: $ZnCo_2O_4$

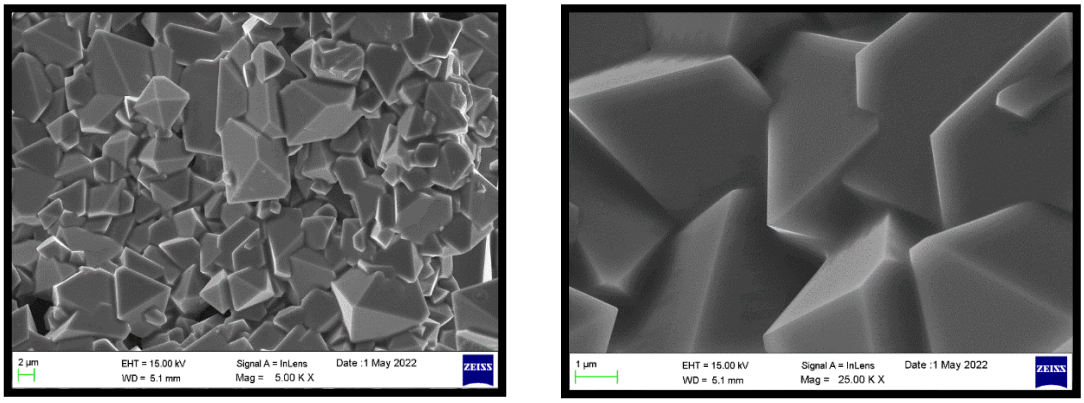

Figure 4.4c: FESEM micrographs of K: $ZnCo_2O_4$

4.6 Cyclic Voltammetry (CV) Analysis

Figure 4.5 a, b and c shows the effect of scan rate on supercapacitor performance of Ba: $ZnCo_2O_4$, Cs: $ZnCo_2O_4$ and K: $ZnCo_2O_4$ devices studied within the potential window of −0.3 to +0.5 V at scan rates of 10–100 mV/s. The current under CV curves slowly increased with scan rate i.e., current is directly proportional to scan rate of CV. The shape of the CV curves of fabricated symmetric supercapacitor device with Ba: $ZnCo_2O_4$, Cs: $ZnCo_2O_4$ and K: $ZnCo_2O_4$ indicating the charge storage mechanism of the device has both electric double layer capacitive and pseudocapacitive behaviour. Further, nature of the CV curve for all the prepared samples show the performance of the device mainly contributed from the redox behaviour of the device.

The cycling performance of symmetric supercapacitor device with Ba: $ZnCo_2O_4$, Cs: $ZnCo_2O_4$ and K: $ZnCo_2O_4$ have been tested for 50 cycles, 100 cycles and 500 cycles at the scan rate of 100 mV/s. The cyclic stability of device with Ba: $ZnCo_2O_4$, Cs: $ZnCo_2O_4$ and K: $ZnCo_2O_4$ for 50 cycles, 100 cycles and 500 cycles at the scan rate of 100 mV/s are given in Figure 4.6 (a-c), 4.7 (a-c) and 4.8 (a-c). Even after 500 consecutive cycles, the shape of the CV curve is maintained for all the devices which indicates the reversibility of all the devices. However, after 500 cycles, the area of the CV curve has been changed from its initial cycle which implies capacity fading of all the three devices. The fading may arise due to the dominant behaviour of redox mechanism in the constructed symmetric devices. However, compared to all the symmetric devices, the device with Ba: $ZnCo_2O_4$ shows low fading which is observed in Figure 4.7 (a-c). In addition to low capacity fading observed in Ba doped Zinc cobaltite symmetric device, the area under the CV curve is higher than the device with Cesium and Potassium doped devices. The higher area under the CV curve represents the higher capacitive behaviour of the Ba: $ZnCo_2O_4$|PVA-KOH| Ba: $ZnCo_2O_4$. The reason for capacity fading and higher capacitance observed in the Ba: $ZnCo_2O_4$|PVA-KOH| Ba: $ZnCo_2O_4$ is given by electrochemical impedance analysis of symmetric supercapacitor device with Ba: $ZnCo_2O_4$, Cs: $ZnCo_2O_4$ and K: $ZnCo_2O_4$.

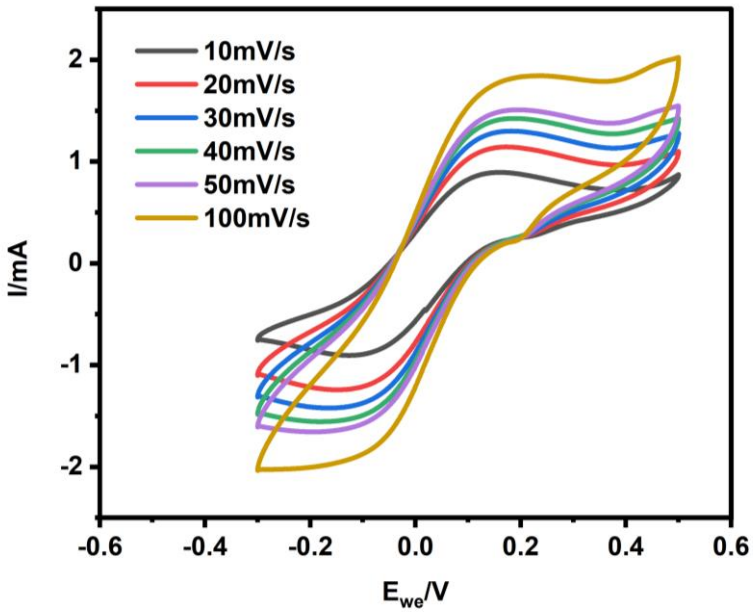

Figure 4.5a: Cyclic voltammetry analysis of Ba: $ZnCo_2O_4$|PVA-KOH| Ba: $ZnCo_2O_4$ symmetric device

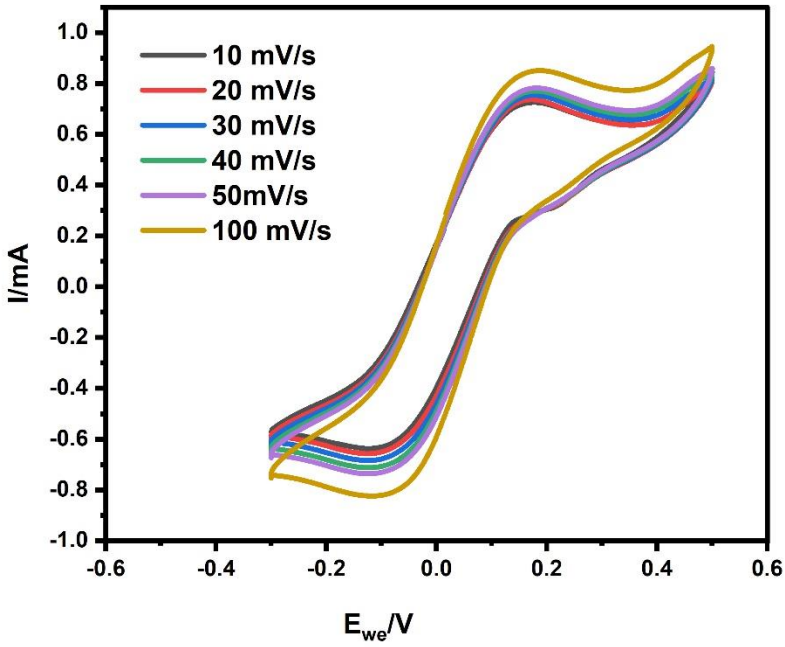

Figure 4.5b: Cyclic voltammetry analysis of Cs: $ZnCo_2O_4$|PVA-KOH| Cs: $ZnCo_2O_4$ symmetric device

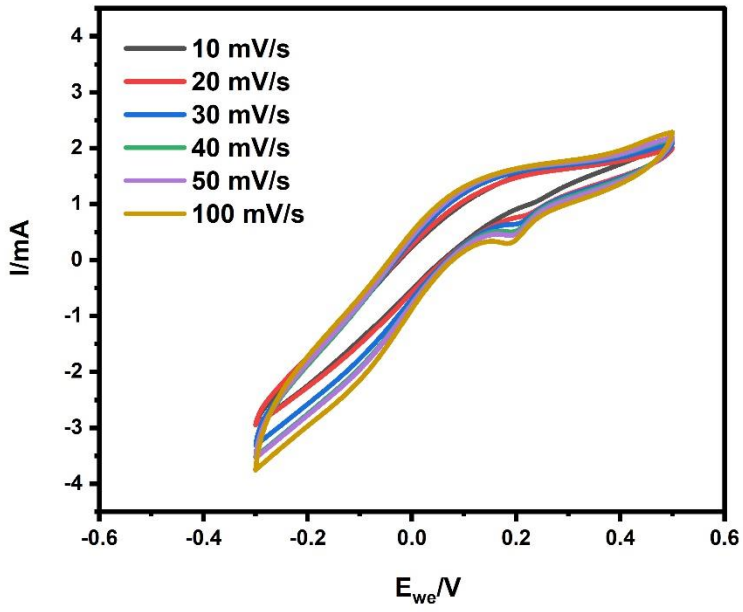

Figure 4.5c: Cyclic voltammetry analysis of K: $ZnCo_2O_4$|PVA-KOH| K: $ZnCo_2O_4$ symmetric device

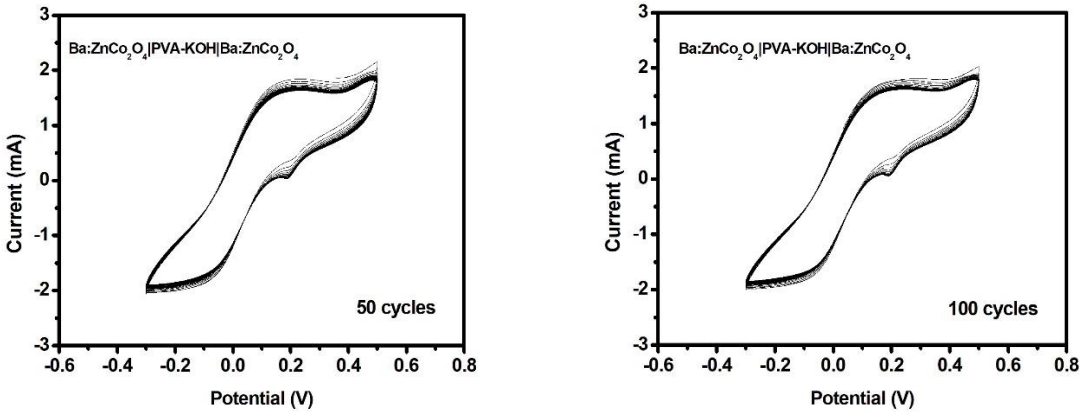

Figure 4.6a and 4.6b: Cyclic voltammetry analysis of Ba: $ZnCo_2O_4$|PVA-KOH| Ba: $ZnCo_2O_4$ symmetric device for 50 and 100 cycles

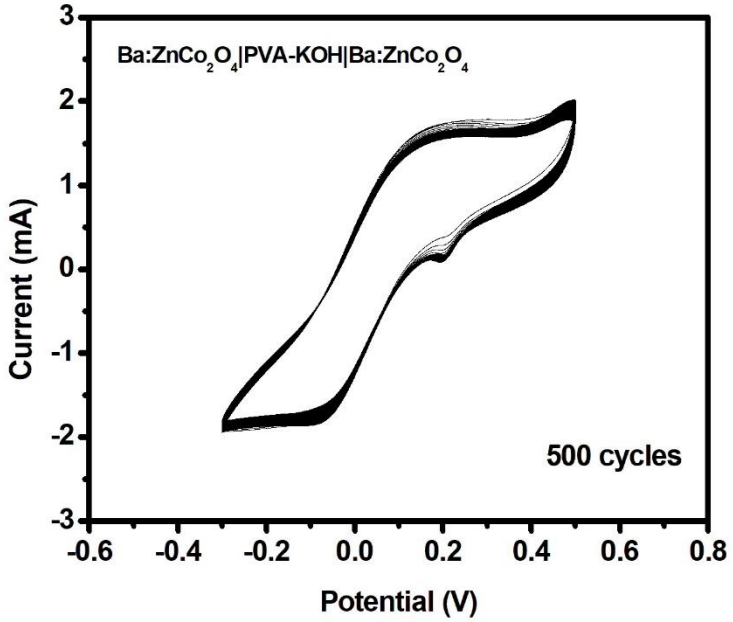

Figure 4.6c: Cyclic voltammetry analysis Ba: $ZnCo_2O_4$|PVA-KOH| Ba: $ZnCo_2O_4$ symmetric device 500 cycles

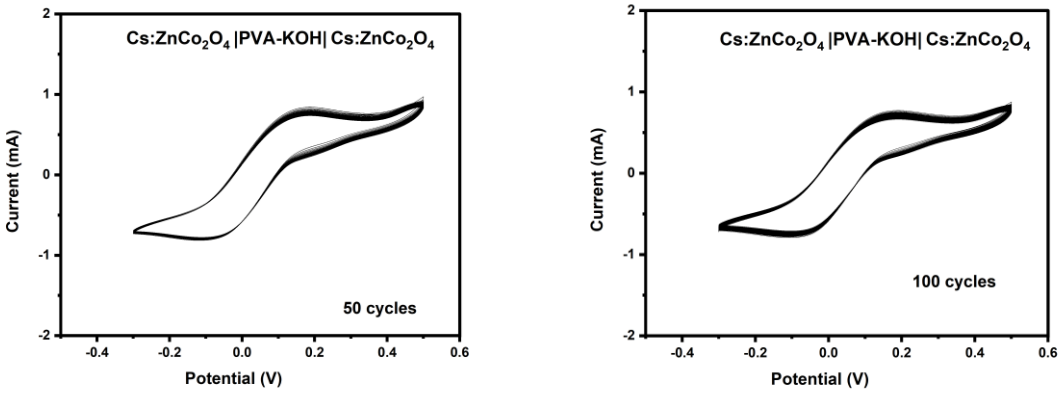

Figure 4.7a and 4.7b: Cyclic voltammetry analysis Cs: $ZnCo_2O_4$|PVA-KOH| Cs: $ZnCo_2O_4$ symmetric device for 50 and 100 cycles

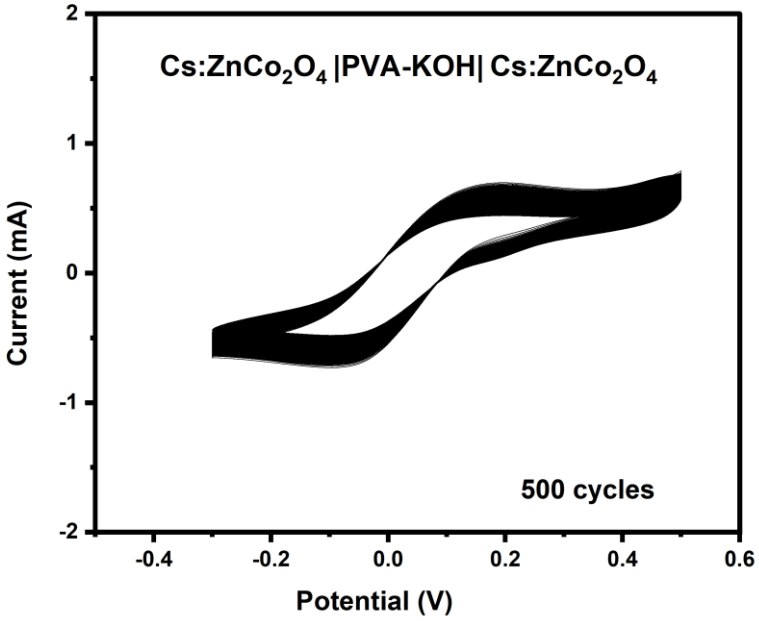

Figure 4.7c: Cyclic voltammetry analysis of Cs: $ZnCo_2O_4$|PVA-KOH| Cs: $ZnCo_2O_4$ symmetric device for 500 cycles

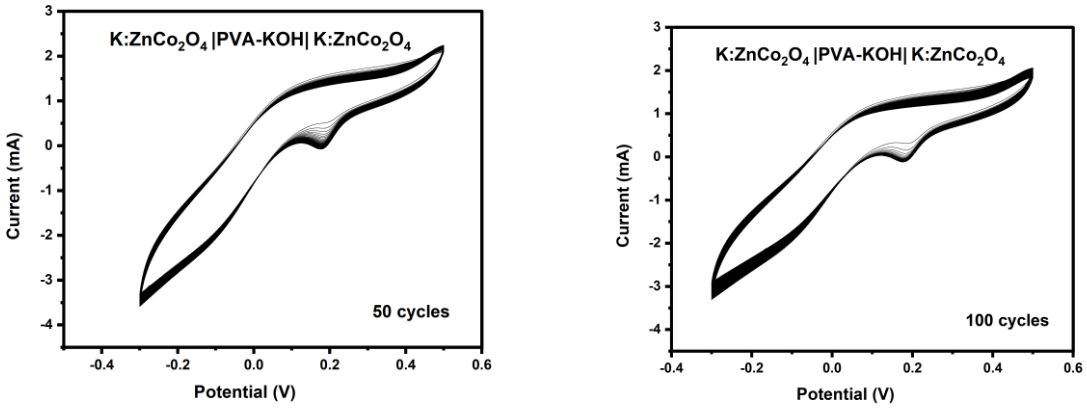

Figure 4.8a and 4.8b: Cyclic voltammetry analysis of K: $ZnCo_2O_4$|PVA-KOH| K: $ZnCo_2O_4$ symmetric device for 50 and 100 cycles

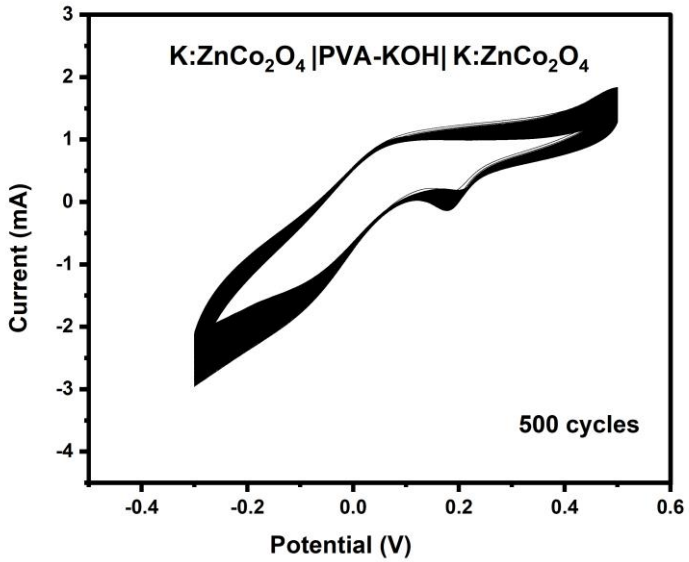

Figure 4.8c: Cyclic voltammetry analysis of K: $ZnCo_2O_4$|PVA-KOH| K: $ZnCo_2O_4$ symmetric device for 500 cycles

4.7. Electrochemical Impedance analysis:

The impedance spectra of device with Ba: $ZnCo_2O_4$, Cs: $ZnCo_2O_4$ and K: $ZnCo_2O_4$ is shown in Figure 4.9, 4.11 and 4.12. It is measured in the range of 10 KHz to 100mHz. The corresponding impedance spectra are fitted by EC lab software by using an equivalent circuit as shown in Figure 4.10 which is the same for all fabricated devices with Ba: $ZnCo_2O_4$, Cs: $ZnCo_2O_4$ and K: $ZnCo_2O_4$. The fitted parameters are given in Table 4.4, 4.5 and 4.6. Before cycling, compared to all the fabricated devices, internal resistance of the Ba doped Zinc cobaltite fabricated device is low. After cycling, the charge transfer resistance is low in the case of Barium based device which may be due to the effective contact between the PVA-KOH electrolyte and Ba: $ZnCo_2O_4$ electrode material. Apart from the resistive components, the equivalent circuit contains constant phase elements. In all the symmetric devices, the existence of CPE and changes in corresponding 'n' values with cycling may be attributed to the distribution of active sites across the sample. In the fabricated device with Ba doped Zinc cobaltite n1 value decreased to 0.1393 (n>0.5) after cycling, indicating the existence of redox behaviour in the symmetric device.

Compared to before cycling, the internal resistance of the fabricated device after cycling in Cs: $ZnCo_2O_4$ and K: $ZnCo_2O_4$ have increased. Hence, the capacity fading has been observed

in the symmetric device with Cs: $ZnCo_2O_4$ and K: $ZnCo_2O_4$. Both before and after cycling, the internal resistances of Ba: $ZnCo_2O_4$ based symmetric device are lower than that of the devices with Cs: $ZnCo_2O_4$ and K: $ZnCo_2O_4$. Due to this, the low capacity fading and higher capacitive behaviour are observed for the Ba: $ZnCo_2O_4$|PVA-KOH| Ba: $ZnCo_2O_4$ symmetric supercapacitor device than other two devices as seen from CV analysis.

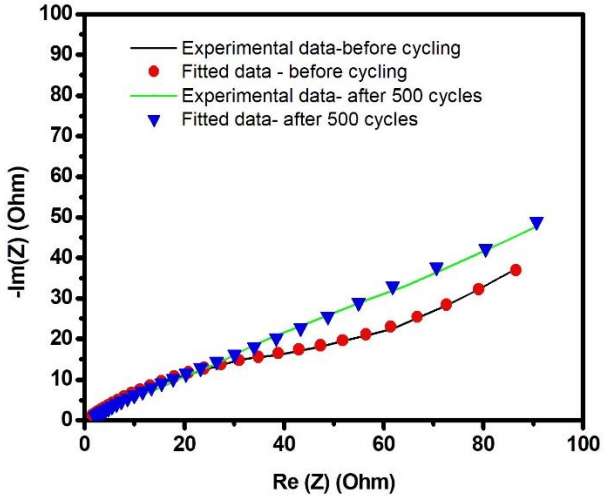

Figure 4.9: Impedance spectra of Ba: $ZnCo_2O_4$|PVA-KOH| Ba: $ZnCo_2O_4$ symmetric device

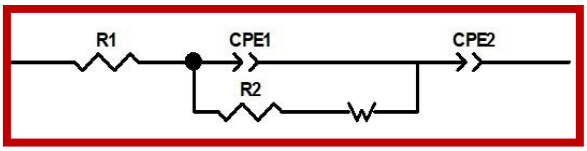

Figure 4.10: Equivalent circuit Ba: $ZnCo_2O_4$|PVA-KOH| Ba: $ZnCo_2O_4$ symmetric device

Table 4.4: Fitted parameters for Ba: $ZnCo_2O_4$|PVA-KOH| Ba: $ZnCo_2O_4$ symmetric device

Sample/Parameters	Before cycling	After cycling
R1(Ω)	1.229	0.2858
R2(Ω)	36.39	10.08
CPE 1	$2.954x10^{-3}$	0.0175
n1	0.5056	0.1393
CPE 2	0.023	0.0246
n2	0.4193	0.482
W	2.471	24.07

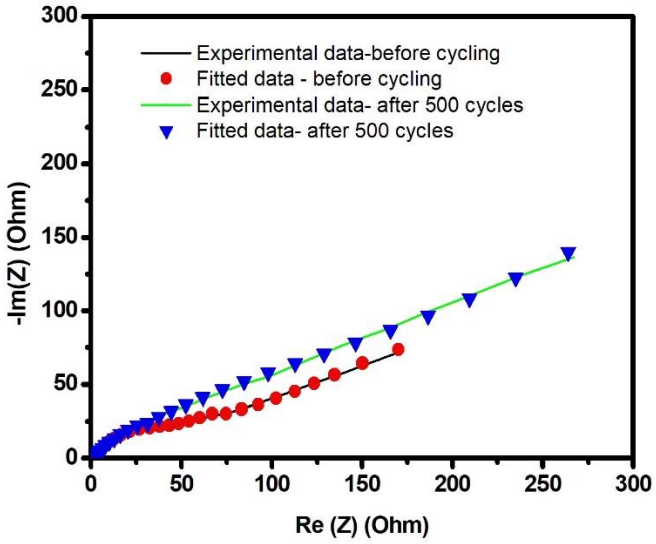

Figure 4.11: Impedance spectra of Cs: $ZnCo_2O_4$|PVA-KOH| Cs: $ZnCo_2O_4$ symmetric device

Table 4.5: Fitted parameters for Cs: $ZnCo_2O_4$|PVA-KOH| Cs: $ZnCo_2O_4$ symmetric device

Sample/Parameters	Before cycling	After cycling
R1(Ω)	1.621	0.4528
R2(Ω)	39.8	110.4
CPE 1	$1.009x10^{-3}$	$2.506x10^{-3}$
n1	0.6713	0.5141
CPE 2	$8.134x10^{-3}$	$5.731x10^{-3}$
n2	0.3353	0.4096
W	1.66	0.453

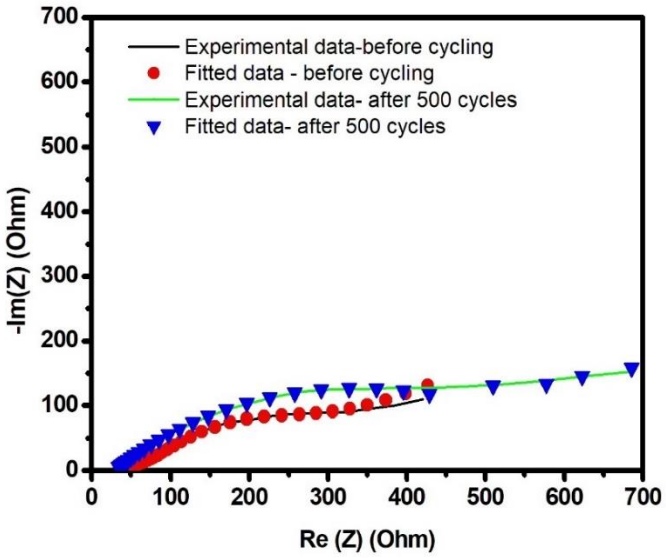

Figure 4.12: Impedance spectra of K: $ZnCo_2O_4$|PVA-KOH|K: $ZnCo_2O_4$ symmetric device

Table 4.6: Fitted parameters for symmetric device with K: $ZnCo_2O_4$

Sample/Parameters	Before cycling	After cycling
R1(Ω)	33.15	28.81
R2(Ω)	135.4	595.8
CPE 1	$0.578x10^{-3}$	$0.535x10^{-3}$
n1	0.727	0.5012
CPE 2	$3.888x10^{-3}$	0.1067
n2	0.229	0.4169
W	27.7	5.337

4.8. Galvanostatic charge-discharge (GCD) analysis:

The capacitive behaviour of the symmetric device is further confirmed by GCD analysis. Figure 4.13a,4.13b and 4.13c shows the GCD analysis of symmetric device with Ba: $ZnCo_2O_4$, Cs: $ZnCo_2O_4$ and K: $ZnCo_2O_4$ at the current densities from 1 Ag^{-1} to 2 Ag^{-1}. All the fabricated symmetric devices show the non-linear nature of the GCD curve indicating redox behaviour of the symmetric supercapacitor device and is supported by CV analysis. From the GCD curves, specific capacitance, energy and power density of the constructed devices have been calculated by using below mentioned relations.

The equation for calculating the specific capacitance from the GCD curve is

$$C = \frac{I\Delta t}{m\Delta V}\ \mathrm{Fg^{-1}} \qquad (4)$$

where,

I– discharge current (A),

Δt- discharge time (s)

ΔV- potential window (V)

The energy density (E) and power density (P) of the device is calculated by the following equations:

$$E = \frac{1}{2} C\,\Delta V^2\ \mathrm{WhKg^{-1}} \qquad (5)$$

$$P = \frac{E}{\Delta t}\ \mathrm{WKg^{-1}} \qquad (6)$$

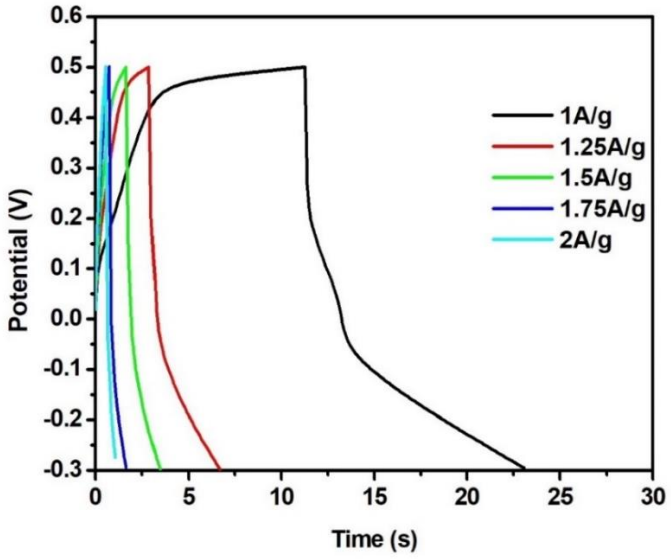

Figure 4.13a: GCD analysis of Ba: $ZnCo_2O_4$|PVA-KOH| Ba: $ZnCo_2O_4$ symmetric device

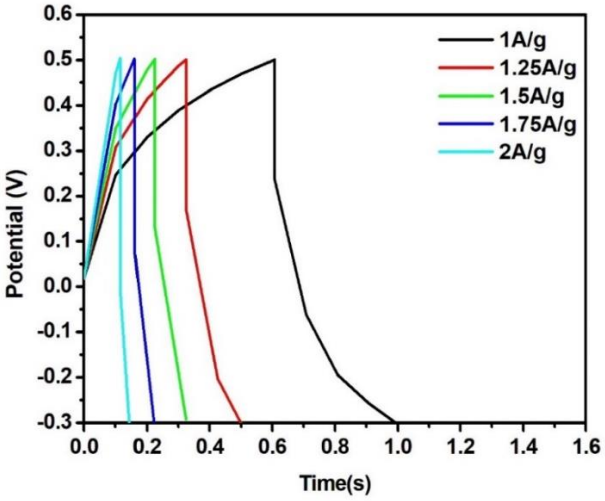

Figure 4.13b: GCD analysis of Cs: $ZnCo_2O_4$|PVA-KOH| Cs: $ZnCo_2O_4$ symmetric device

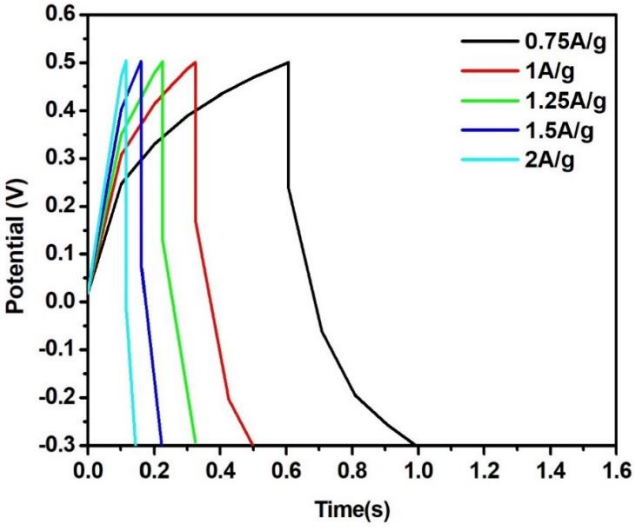

Figure 4.13c: GCD analysis of K: $ZnCo_2O_4$|PVA-KOH| K: $ZnCo_2O_4$ symmetric device

Table 4.7 shows the specific capacitance, energy density and power density of symmetric devices with Ba: $ZnCo_2O_4$, Cs: $ZnCo_2O_4$ and K: $ZnCo_2O_4$ electrode material. From the Table 4.7, it is concluded that the higher specific capacitance value of all the fabricated symmetric devices is reached at the current density of 1 Ag^{-1}. This is due to the rapid redox behaviour at high scan rates in which there is no sufficient time available for ion transportation following the behaviour of the undoped sample. A among all the fabricated devices, Barium doped Zinc cobaltite based symmetric device exhibits higher specific capacitance of 14.66 Fg^{-1} at the current density of 1 Ag^{-1}. It is attributed to the lowest internal resistance of the device and as discussed in the impedance analysis. Hence, Ba: $ZnCo_2O_4$|PVA-KOH| Ba:

$ZnCo_2O_4$ symmetric device shows higher energy density (1.3 $WhKg^{-1}$) with a power density of 400 W Kg^{-1} than other devices.

Table 4.7: Specific capacitance, Energy density and Power density of symmetric device with Ba: $ZnCo_2O_4$, Cs: $ZnCo_2O_4$ and K: $ZnCo_2O_4$ electrode material

Sample	Current density (Ag^{-1})	Specific capacity (Fg^{-1})	Energy density ($Whkg^{-1}$)	Power density (Wkg^{-1})
Ba: $ZnCo_2O_4$	1	14.66	1.30	400
	1.25	5.98	0.53	500
	1.50	3.36	0.29	600
	1.75	1.96	0.17	700
	2	1.42	0.12	800
Cs: $ZnCo_2O_4$	1	0.36	0.032	400
	1.25	0.18	0.016	500
	1.50	0.12	0.010	600
	1.75	0.08	0.007	700
	2	0.07	0.006	800
K: $ZnCo_2O_4$	1	0.47	0.042	400
	1.25	0.26	0.023	500
	1.50	0.19	0.017	600
	1.75	0.12	0.010	700
	2	0.07	0.006	800

CHAPTER – 5

SUMMARY AND CONCLUSION

Barium doped Zinc cobaltite, Cesium doped Zinc cobaltite and Potassium doped Zinc cobaltite are prepared using sol-gel method. The prepared material Ba: $ZnCo_2O_4$, Cs: $ZnCo_2O_4$ and K: $ZnCo_2O_4$ possess spinel structure with crystallite size of 52nm, 34nm, 34nm. Raman result shows the formation of spinel structure of Ba, Cs and K doped Zinc cobaltite. FT-IR result shows the stretching modes of Co-O and Zn-O and conforms the formation of $ZnCo_2O_4$. Ba being a divalent element, on doping the site occupation seems to get exchanged within the A-O-B sites that is understood by FTIR results and the DFT reports published already on several other dopants. FESEM shows micrographs of Ba: $ZnCo_2O_4$, Cs: $ZnCo_2O_4$ and K: $ZnCo_2O_4$ reveal the spinel shaped and assorted grain size formation. The grain size of all the prepared sample is in micrometer range due to agglomeration of smaller crystallites as seem in XRD. In Cyclic Voltammetry (CV) Analysis, the shape of the CV curves of fabricated symmetric supercapacitor device with Ba: $ZnCo_2O_4$, Cs: $ZnCo_2O_4$ and K: $ZnCo_2O_4$ indicates the charge storage mechanism of the device has both electric double layer capacitive and pseudocapacitive behaviour. After 500 cycles, the impedance spectra of Ba: $ZnCo_2O_4$, Cs: $ZnCo_2O_4$ and K: $ZnCo_2O_4$ is measured in the range of 10 KHz to 100mHz. Compared to Cs: $ZnCo_2O_4$ and K: $ZnCo_2O_4$ symmetric device, Ba: $ZnCo_2O_4$ symmetry device exhibits lower internal resistance value. Hence, the low capacity fading has been observed in the symmetric device constructed with Ba: $ZnCo_2O_4$. Galvanostatic charge-discharge (GCD) analysis confirmed the capacitive behaviour of the symmetric device. The calculated energy and power density of the device, Ba: $ZnCo_2O_4$, is 1.3 $WhKg^{-1}$ at 400 WKg^{-1}. Compared with Cs: $ZnCo_2O_4$ and K: $ZnCo_2O_4$ symmetric device, Ba: $ZnCo_2O_4$ is more suitable and effective material for symmetric supercapacitor applications.

References

1.**Ganesh Koyyada, Nadavala Siva Kumar, Ibrahim H. Al. Ghurabi, Mourad Boumaza, Jae Hong Kim and Koduru Mallikarjuna**; In situ microwave-assisted solvothermal synthesis via morphological transformation of ZnCo2O4 3D nanoflowers and nanopetals to 1D nanowires for hybrid supercapacitors; Royal Society of Chemistry, Vol. 11, Article. 5928, (2021). DOI: 10.1039/d0ra09507a.

2.https://www.powerelectronics.com/technologies/alternativeenergy/article/21864122/superc a pacitors-past-present-and-future

3. **Kumcham Prasad, Gutturu Rajasekhara Reddy, Megala Rajesh, P. Reddi Babu, Gnanendra Shanmugam, N. John Sushma, M. Siva Pratap Reddy, Borelli Deva Prasad Raju and Koduru Mallikarjuna;** Electrochemical Performance of 2D-HierarchicalSheetLike ZnCo2O4 Microstructures for Supercapacitor Applications; Crystals, Vol. 10, Article no. 566, (2020).

4.**T.V.M. Sreekanth, P.C. Nagajyothi, K. C. Devarayapalli, J. Shim and K. Yoo**; Lilac flower-shaped $ZnCo_2O_4$ electrocatalyst for efficient methanol oxidation and oxygen reduction reactions in alkaline medium; Cryst Eng Comm, vol.22, pp:2849-2858, (2020) DOI: 10.1039/D0CE00024H.

5. **Zi wen Wang, Shixiang Lu, Ge He, Anqi Lv, Yanmei Shen and Wenguo Xu**; In situ construction of dual-morphology $ZnCo_2O_4$ for high-performance asymmetric supercapacitors; Nanoscale Adv**,** vol.8, pp: 3086-3094, (2019) DOI: 10.1039/c9na00230h.

6. **Swati J Patil, Jungsung Park and Dong-Weon Lee**; Facial synthesis of nanostructured $ZnCo_2O_4$ on carbon cloth for supercapacitor application; Mater Sci Eng, Vol.281, pp:282-29, (2019) DOI:10.1088/1757-899X/282/1/012004.

7. **Harsharaj S. Jadhav, Animesh Roy, Wook-Jin Chung, Jeong Gil Seo**; Growth of urchin-like $ZnCo_2O_4$ microspheres on nickel foam as a binder free electrode for high-performance supercapacitor and methanol electrooxidation**;** Electrochimica Acta, vol.246, pp: 941-950, (2017) DOI: 10.1016/j.electacta.2017 .06.118.

8. **Jian Bao, Zhaolong Wang, Wenjun Liu, Li Xu, Fengcai Lei, Junfeng Xie, Yan Zhao, Yunpeng Huang, Meili Guan, Huaming Li**; $ZnCo_2O_4$ ultrathin nanosheets towards the high performance of flexible supercapacitors and bifunctional electrocatalysis; Journal of Alloys and Compounds, vol.764, pp:565-573, (2018) DOI: 10.1016/j.jallcom.2018.06.085.

9**. De yang Yu, Ziqing Zhang, Ya'nan Meng, Yifei Teng, Yunpeng Wu, Xinyang Zhang, Qiushi Sun, Wenming Tong, and Xiaoyang Liu**; The Synthesis of Hierarchical $ZnCo_2O_4$@MnO_2 Core-Shell Nanosheet Arrays on Ni Foam for High-Performance All-Solid-State Asymmetric Supercapacitors**;** Inorg. Chem. Front**,** vol.5, pp: 597-604, (2017) DOI: 10.1039/C7QI00706J.

10. **Sumanta Sahoo and Jae-Jin Shim;** Facile Synthesis of 3D Ternary $ZnCo_2O_4$/Reduced Graphene Oxide/Ni O Composite Film on Nickel Foam for Next Generation Supercapacitor Electrodes; ACS Sustainable Chem Eng, vol.1, pp: 241–251, (2016) DOI: 10.1021/acssuschemeng.6b01367.

11. **Gracita M. Tomboc, Harsharaj S. Jadhav, Hern Kim**; PVP assisted morphology-controlled synthesis of hierarchical mesoporous $ZnCo_2O_4$ nanoparticles for high-performance pseudo capacitor; Chemical Engineering Journal, (2016) DOI: 10.1016/j.cej.2016.09.056.

12. **Le Xu, Yan Zhao, Jiabiao Lian, Yuanguo Xu, Jian Bao, Jingxia Qiu, Li Xu, Hui Xu, Mingqing Hua, Huaming L**; Morphology controlled preparation of $ZnCo_2O_4$ nanostructures for asymmetric supercapacitor with ultrahigh energy density; Energy, vol.123 pp*:* 296-304, (2017) DOI: 10.1016/j.energy.2017.02.018.

13. **Lingyun Guo, Qiang Ru, Xiong Song, Shejun Hu, Yudi Mo**; Mesoporous $ZnCo_2O_4$ microspheres as anode material for high-performance secondary lithium-ion batteries; RSC Adv, vol.5, pp: 19241-19247, (2015) DOI: 10.1039/C4RA15553J.

14. **Chun Wu, Junjie Cai , Qiaobao Zhang, Xiang Zhou, Ying Zhu, Lingjun Li, Peikang Shen, Kaili Zhang**; Direct growth of urchin-like $ZnCo_2O_4$ microspheres assembled from nanowires on nickel foam as high-performance electrodes for supercapacitors; Electrochimica Acta., vol.169, pp: 202-209, (2015) DOI: 10.1016/j.electacta.2015.04.079.

15**. Liang Huang, Gordon Henry Waller, Yong Ding, Dongchang Chena, Dong Ding, Pinxian Xi, Zhong Lin Wang, Meilin Liu**; Controllable interior structure of $ZnCo_2O_4$ microspheres for high-performance lithium-ion batteries; Nano Energy, vol.11, pp: 64-70, (2014) DOI: 10.1016/j.nanoen.2014.09.027.

16. **Lingyun Guo, Qiang Ru, Xiong Song, Shejun Hu and Yudi Mo**; Pineapple-shaped $ZnCo_2O_4$ microspheres as anode materials for lithium ion batteries with prominent rate performance; J. Mater. Chem, vol.3, pp:8683–8692, (2014) DOI: 10.1039/c5ta00830a.

17. **Bin Liu, Bin Liu, Boyang Liu, Qiufan Wang, Xianfu Wang, Qingyi Xiang, Di Chen, and Guozhen Shen**; New Energy Storage Option: Toward $ZnCo_2O_4$ Nanorods/Nickel Foam Architectures for High- Performance Supercapacitors; ACS Appl. Mater, vol.5, pp: 10011-7, (2013) DOI: 10.1021/am402339d.

18. **Fuxi Bao, Xiaofeng Wang, Xudong Zhao, Ying Wang, Ying Ji, Hongdan Zhang and Xiaoyang Liu**; Controlled growth of mesoporous $ZnCo_2O_4$ nanosheet arrays on Ni foam as high-rate electrodes for supercapacitors; RSC Adv, vol.4, pp*:* 2393-2397, (2014) DOI: 10.1039/c3ra46439c.

19. **Ganesh Koyyada, Nadavala Siva Kumar, Ibrahim H. Al. Ghurabi, Mourad Boumaza, Jae Hong Kim and Koduru Mallikarjuna**; In situ microwave-assisted solvothermal synthesis via morphological transformation of ZnCo2O4 3D nanoflowers and nanopetals to 1D nanowires for hybrid supercapacitors; Royal Society of Chemistry, Vol. 11, Article. 5928, (2021). DOI: 10.1039/d0ra09507a.

20. **M. Priya, V.K. Premkumar, P. Vasantharani, G. Sivakumar**; Structural and electrochemical properties of $ZnCo_2O_4$ nanoparticles synthesized by hydrothermal method; Vacuum, vol.167, pp:307-312, (2019) DOI: 10.1016/j.vacuum.2019.06.020.

21. **Kumcham Prasad, Gutturu Rajasekhara Reddy, Megala Rajesh, P. Reddi Babu, Gnanendra Shanmugam, N. John Sushma, M. Siva Pratap Reddy, Borelli Deva Prasad Raju and Koduru Mallikarjuna;** Electrochemical Performance of 2D-Hierarchical SheetLike $ZnCo_2O_4$ Microstructures for Supercapacitor Applications; Crystals, Vol 10, Article no. 566, (2020).

22. **Yueshen zhou, Liang Chen, YueTing Jiao, Zhaolei Li, Yanmin Gao**; Controllable fabrication of $ZnCo_2O_4$ ultra-thin curved sheets on Ni foam for high-performance asymmetric supercapacitors; Electrochimica Acta, vol.299, pp: 388-394, (2018), DOI: 10.1016/j.electacta.2018.12.186.

23. **Yuanyuan Shang, Tian Xie, Chuanli Ma, Linghao Su, Yansong Gai, Jing Liu, Liangyu Gong**; Synthesis of hollow $ZnCo_2O_4$ microspheres with enhanced electrochemical performance for asymmetric supercapacitor; Electrochimica Acta, vol.286, pp: 103-113, (2018) DOI: 10.1016/j.electacta.2018.08.025.

24. **Li Xie, Yu Liu, Hongye Bai, Chunxiang Li, Baodong Mao, Lin Sun, Weidong Shi**; Core-shell structured $ZnCo_2O_4$@ZnWO4 nanowire arrays on nickel foam for advanced asymmetric supercapacitors*;* Journal of Colloid and Interface Science, vol.531, pp: 64-73, (2018) DOI: 10.1016/j.jcis.2018.07.049.

25. **Jikui Zhu, u, Dianmei Song, Tao Pu, Jie Li, Biao Huang, Wensong Wang, Chenglan Zhao, Li Xie, Lingyun Chen**; Two-dimensional Porous $ZnCo_2O_4$ Thin Sheets Assembled by 3D Nanoflake Array with Enhanced Performance for Aqueous Asymmetric Supercapacitor; Chemical Engineering Journal, vol.336, , pp: 679-689, (2017) DOI: 10.1016/j.cej.2017.12.035.

26. **Katong Liu, Xiaodong Li, Liang Liang, Ju Wu, Xingchen Jiao, Jiaqi Xu, Yongfu Sun and Yi Xie;** Ni-doped ZnCo2O4 atomic layers to boost the selectivity in solar-driven reduction of CO2; Nano Research, Vol. 11, pp . 2897–2908, (2018)

27. **Xiangwen Ma, Peng Zhang, Yuanyuan Zhao, Ying Liu, Jian Li, Jin Yuan Zhou, Xiaojun Pan, Erqing Xie**; Role of N doping on the electrochemical performances of $ZnCo_2O_4$ quantum dots/reduced graphene oxide composite nanosheets; Chemical Engineering Journal, vol.327, pp:1000-1010, (2017) DOI: 10.1016/j.cej.2017.06.084.

28. **Yu Pan, , Hong Gao, Mingyi Zhang, Lu Li, Guangning Wang, Xinyuan Shan**; Three-dimensional porous $ZnCo_2O_4$ sheet array coated with Ni $(OH)_2$ for high performance asymmetric supercapacitor; Journal of Colloid and Interface Science, vol.497, pp:50-56, (2017) DOI: 10.1016/j.jcis.2017.02.053.

29. **V. Venkatachalam, A. Alsalme, A. Alswieleh, R. Jayavel;** Double hydroxide mediated synthesis of nanostructured $ZnCo_2O_4$ as high-performance electrode material for supercapacitor applications; Chemical Engineering Journal, Vol. 321, pp: 474 – 483, (2017).

30. **In Kyu Moon, Seonno Yoon, and Jungwoo Oh**; 3D Hierarchically Mesoporous $ZnCo_2O_4$ Nanowires Grown on Graphene/Sponge Foam for High Performance Flexible All-Solid-State Supercapacitors; A European journal, vol.23, pp:597-604, (2016) DOI: 10.1002/chem.201602447.

31. **De yang Zhang, Yihe Zhang, Xiaowei Li, Yongsong Luo, Hongwei Huang, Jiaping wang and Paul K. Chu**; Self-assembly of Mesoporous $ZnCo_2O_4$ Nanomaterials: Density Functional Theory Calculation and Flexible All-Solid-State Energy Storage**;** J. Mater. Chem. A, issue:2, pp:568-577, (2015) DOI: 10.1039/C5TA07105D.

32. **Gang Zhou, , Jian Zhu, Yuejiao Chen, Lin Mei, Xiaochuan Duan, Guanhua Zhang, Libao Chen, Taihong Wang, Bingan Lu**; Simple method for the preparation of highly porous $ZnCo_2O_4$nanotubes with enhanced electrochemical property for supercapacitor; Electrochimica Acta, vol.123, pp: 450-455, (2014) DOI: 10.1016/j.electacta.2014.01.018.

33. **Bing kun Guan, Di Guo, Lingling Hu, Guanhua Zhang, Tao Fu, Weiji Ren, Jidong Li and Qiuhong Li**; Facile synthesis of $ZnCo_2O_4$ nanowire cluster arrays on Ni foam for high-performance asymmetric supercapacitors; J. Mater. Chem. A, issue:38, pp: 16116-16123, (2014) DOI: 10.1039/c4ta02378a.

34**. Parnia Forouzandeh ,Vignesh Kumaravel and Suresh C. Pillai ;** Electrode Materials for Supercapacitors: A Review of Recent Advances; Catalysts, vol. 10, pp: 969, (2020) DOI: 10.3390/catal10090969

35. **Nusrat Shaheen, Muhammad Asif Yousuf, Imran Shakir, Philips Olaleye Agboola and Muhammad FarooqWarsi;** Wet chemical route synthesis of spinel oxide nano-catalysts for photocatalytic applications; Physica B: Condensed Matter, vol. 550, (2020)

36. **G.G. Soundarya, B. Nalini, D. Lakshmi, P. Priyanka**; Structural rearrangement by Ni, Cr doping in zinc cobaltite and its influence on supercapacitance; Ceramics International, vol.47, pp. 18635-18645 (2021) DOI: https://doi.org/10.1016/j.ceramint.2021.03.195